New insights on Titan's plasma-driven Schumann resonance inferred from Huygens and Cassini data

C. Béghin [a,*], P. Canu [b], E. Karkoschka [c], C. Sotin [d], C. Bertucci [e], W.S. Kurth [f],
J.J. Berthelier [g], R. Grard [h], M. Hamelin [g], K. Schwingenschuh [i], F. Simões [g]

[a] *LPC2E-CNRS-Université d'Orléans, 3A, Av. Recherche Scientifique, 45071 Orléans Cedex 2, France*
[b] *CETP-IPSL-Université de Versailles-Saint Quentin en Yvelines, 78140 Vélizy-Villacoublay, France*
[c] *Lunar and Planetary Laboratory, University of Arizona, Tucson, AZ 85721-0092, USA*
[d] *Jet Propulsion Laboratory and California Institute of Technology, Pasadena, CA 91109, USA*
[e] *Institute for Astronomy and Space Physics (IAFE)–CONICET, University of Buenos Aires, Buenos Aires, Argentina*
[f] *Department of Astronomy, University of Iowa, Iowa City, IA 52242, USA*
[g] *CETP-IPSL, 4 Avenue de Neptune, 94107 Saint Maur Des Fossés, France*
[h] *RSSD, ESA-ESTEC, European Space Agency, Keplerlaan 1, 2200 AG Noordwijk, The Netherlands*
[i] *Space Research Institute, Austrian Academy of Sciences (IWF), Schmiedlstrasse 6, 8082 Graz, Austria*

ARTICLE INFO

ABSTRACT

After a preliminary analysis of the low-frequency data collected with the electric antenna of the Permittivity, Wave and Altimetry (PWA) experiment onboard the Huygens Probe that landed on Titan on 14 January, 2005, it was anticipated in a previous article [Béghin et al., 2007. A Schumann-like resonance on Titan driven by Saturn's magnetosphere possibly revealed by the Huygens Probe. Icarus, 191, 251–266] that the Extremely Low-Frequency (ELF) signal at around 36 Hz observed throughout the descent, might have been generated in the upper ionosphere of Titan, driven by a plasma instability mechanism associated with the co-rotating Kronian plasma flow. The involved process was proposed as the most likely source of a Schumann resonance in the moon's atmospheric cavity, the second eigenmode of which is actually found by models to occur at around 36 Hz. In this paper, we present a thorough analysis of this signal based upon the Huygens Probe attitude data deduced from the Descent Imager Spectral Radiometer (DISR), and relevant measurements obtained from the Radio Plasma Wave Science (RPWS) experiment and from the magnetometer (MAG) onboard Cassini orbiter during flybys of Titan. We have derived several coherent characteristics of the signal which confirm the validity of the mechanism initially proposed and provide new and significant insights about such a unique type of Schumann resonance in the solar system. Indeed, the 36 Hz signal contains all the characteristics of a polarized wave, with the measured electric field horizontal component modulated by the antenna rotation, and an altitude profile in agreement with a Longitudinal Section Electric (LSE) eigenmode of the atmospheric cavity. In contrast to Earth's conditions where the conventional Transverse Magnetic mode is considered, the LSE mode appears to be the only one complying with the observations and the unexpected peculiar conditions on Titan. These conditions are essentially the lack of any lightning activity that can be ascertained from Cassini observations, the presence of an ionized layer centered around 62 km altitude that was discovered by the PWA instrumentation, and the existence of a subsurface conducting boundary which is mandatory for trapping ELF waves. A simple theoretical model derived from our analysis places tentatively consequential constraints on the conductivity profile in the lower ionosphere. It is also consistent with the presence of a conductive water ocean below an icy crust some tens of kilometers thick.

© 2009 Elsevier Ltd. All rights reserved.

1. Introduction

Electric field measurements were performed in an extremely low- and very low-frequency ranges (ELF–VLF) with the Permittivity, Waves and Altimetry (PWA) analyzer (see Grard et al., 2006 for overview of preliminary results), as a subsystem of the Huygens Atmospheric Structure Instrument (HASI)

* Corresponding author. Tel.: +33 2 38 25 52 57; fax: +33 2 3863 12 34.
  E-mail address: cbeghin@cnrs-orleans.fr (C. Béghin).

(Fulchignoni et al., 2002) that landed on Titan on January 14, 2005. One electric component of electromagnetic waves was measured with a dipole made of two electrodes separated by about 2 m with the Huygens Probe body in between, which reduces accordingly the effective length to about 1.6 m. In addition to passive observations of waves in the ELF and VLF ranges, the package included the active Mutual Impedance (MI) instrument that used the same dipole and measured the local electron conductivity.

The latter instrument, together with the Relaxation Probe (RP) also installed on the PWA booms, made possible the discovery of a conducting layer at the unexpected low altitude of 60–70 km, attributed to complex ionization–recombination processes driven by both solar ultraviolet and cosmic-ray radiations (Hamelin et al., 2007; Löpez-Moreno et al., 2008). Before Huygens, the theoretical models predicted that the maximum cosmic-ray ionization rate occurred between 100 km (Borucki et al., 1987) and 65 km (Molina-Cuberos et al., 1999). Moreover, the profiles of conductivity and electron concentration found with the models were much less sharpened than the PWA layer, even considering aerosols effect and day-time conditions (Borucki et al., 2006). We are expecting that a new examination of photoemission threshold of aerosols, ultraviolet solar flux and recombination mechanisms, as proposed recently by Borucki and Whitten (2008), ought to allow improving the models after Huygens and Cassini findings. Although the low-altitude peak of conductivity may not be strictly linked to that of maximum of ionization rate from galactic cosmic rays (GCR), the thin conductivity layer around 65 km will be named GCR here, for short and in contrast to the regular ionosphere.

In addition to the discovery of that layer, an intriguing signal appearing in the ELF data as a quasi-monochromatic line, a few Hz wide, centered at around 36 Hz and present almost continuously throughout the descent, has been investigated by Simões et al. (2007) and Béghin et al. (2007). Among several possibilities of instrumental or natural origin, these authors concluded that the observed signal might have been the second eigenmode of a Schumann-like resonance in Titan's atmospheric cavity, with a noticeable specificity with respect to the well-known Schumann resonance on Earth (Schumann, 1952; for a historical review see Besser, 2007).

On Earth, the energy source for triggering the eigenmodes of the cavity is known to be essentially that of powerful atmospheric lightning activity, particularly that coming from return stroke discharges between clouds and the ground. Such a source seems unlikely on Titan since no signature of any kind of electric activity in the atmosphere has been unambiguously detected to date (Fischer et al., 2007), in contrast to Saturn and several other planets (for a review see Yair et al., 2008). Moreover, even by assuming the existence of different kinds of lightning such as corona discharges with individual energy well below the detection threshold (10 kJ) of the Radio Plasma Wave Science (RPWS) experiment onboard Cassini (Lammer et al., 2001), an unlikely continuous rate over 10^5 s^{-1} would be necessary to comply with the observed strength of the PWA signal (Béghin et al., 2007). Nevertheless, evidence of electrical activity in Titan's atmosphere has been recently claimed (Morente et al., 2008) to be the source of several harmonics of a terrestrial-like Schumann resonance. Morente et al. (2008) draw their conclusion from a late-time analysis technique applied to compressed telemetry data files of PWA. In pursuance of a better knowledge of the experiment, the Huygens–PWA team members have expressed recently (Hamelin et al., 2009) several reasons for not endorsing that kind of methodology, which is shown to be irrelevant in that particular case. Hamelin et al. (2009) therefore dispute the analysis proposed by Morente et al. (2008), which leads to the conclusion

that the atmospheric electrical activity and the associated Schumann resonances would be of the same nature on Titan and on Earth. Related technical issues are discussed in more detail in the next section.

As a follow-up of the previous work by Béghin et al. (2007), we present here a much more extensive statistical analysis of the 36 Hz signal extracted from the PWA data which confirms our first interpretation. New insights allow us to draw the basis of a preliminary theoretical model which complies with both PWA measurements and recent observations during Titan flybys by the Cassini spacecraft.

2. The PWA "36 Hz" signal

2.1. The ELF raw data

Since the technical aspects of PWA data processing appear as an important issue, we recall how the ELF raw data are dispatched in telemetry files. The onboard processing of the waveform received by the electric dipole used the discrete Fourier transform (DFT) technique, within a so-called "Schumann" band (3–96 Hz), in two pre-programmed modes of operation (for details see Grard et al., 1995). The first mode, starting at 156 s mission time (MT) at around 141 km altitude until 1926 s MT (~61 km), was designed to provide 32 frequency bins giving 3 Hz resolution. At 1930 s MT the PWA was switched to the second mode until the surface was reached, with 16 bins each of 6 Hz resolution. Due to the loss of the second channel in the radio relay between Huygens and Cassini (Lebreton et al., 2005), only half the data was received, i.e., the 16 even bins by steps of 6 Hz during the first period and 8 even bins by steps of 12 Hz in the second period. Fortunately, the stronger signal observed during the descent (Grard et al., 2006; Béghin et al., 2007; Simões et al., 2007) occurs in the 36 Hz bin which is common to both modes of operation. Here, we make use of only 3 bins at 24, 36 and 48 Hz throughout the descent. The overall ELF spectral shape in that range and on each side essentially displays a typical decreasing slope close to $1/f$, plus a significant bump at around the 36 Hz bin of high variable strength (Simões et al., 2007). On some occasions this signal is quite noisy, but it is nevertheless always detectable during the descent. From this particular feature, we have used a simple analytical procedure to extract a so-called "36 Hz signal" from the ambient broadband ELF noise. By using the 2 bins at 24 and 48 Hz which provide the background shape for the wideband spectrum, one may fit each pair of temporal samples with a theoretical law of the form a/f^b where a and b are two variables determined by the following relations:

$$b = \frac{1}{\log 2} \log\left[\frac{\text{VADC}_{24}}{\text{VADC}_{48}}\right]; \quad a = (24)^b \text{VADC}_{24} = (48)^b \text{VADC}_{48} \quad (1)$$

where VADC_f is the input rms voltage of the Analogue–Digital Converter, obtained by decompressing the raw telemetry data. This quantity is proportional to the square root of power spectral density of the antenna voltage within the bin of frequency f (Jernej and Falkner, 2004). Then, both components at 36 Hz are extracted by assuming that they are not correlated, so we get

$$\text{ELF}_{36} = \frac{a}{36^b}; \quad X = \sqrt{\text{VADC}_{36}^2 - \text{ELF}_{36}^2} \quad (2)$$

where ELF_{36} and X are the equivalent VADC amplitudes at 36 Hz of the broadband ELF noise and of the extracted signal, respectively.

2.2. Altitude profile of the extracted signals

The above processing was performed on segments of 100 or 50 spectral values corresponding to about 300 or 150 s throughout the descent, to obtain smoothed values and running means before and after particular events, such as parachute release inflation and PWA mode change. The altitude profiles of average values of extracted components and the coefficients a and b of the ELF noise spectrum are plotted in Fig. 1. From these profiles we may identify four different portions whose specific characteristics are summarized below

(i) The first portion, from the beginning of the measurements until the main parachute release (140–111 km, MT 156–898 s), is characterized by very low amplitudes of both components (Fig. 1, upper panel). Moreover, with b nearly equal to 1 (lower panel), the ELF power spectrum resembles more of random bursts due to an instrumental interference

than that of a natural signal. The overall level is very similar indeed to that observed during the cruise phase (Simões et al., 2007; Hamelin et al., 2009). This point is illustrated by the first four spectra collected during the cruise checkout #10 shown in Fig. 2 (top panel), together with the first raw power spectrum acquired during the descent, the same sample which was selected for a case study by Morente et al. (2008). We have been able to reproduce the features interpreted as resonances by Morente et al. (2008), using the late-time analysis method in the same conditions. We have retrieved indeed the alleged resonances of the considered case study (Fig. 2, bottom panel). We claim nevertheless that this approach is not appropriated to the Huygens–PWA data (Hamelin et al., 2009), since the same procedure applied to the cruise-phase data yields similar peaks randomly distributed in amplitude and frequency, as shown in Fig. 2. This demonstration shows that the data obtained during the initial part of the Huygens descent, from 140 down to 110 km,
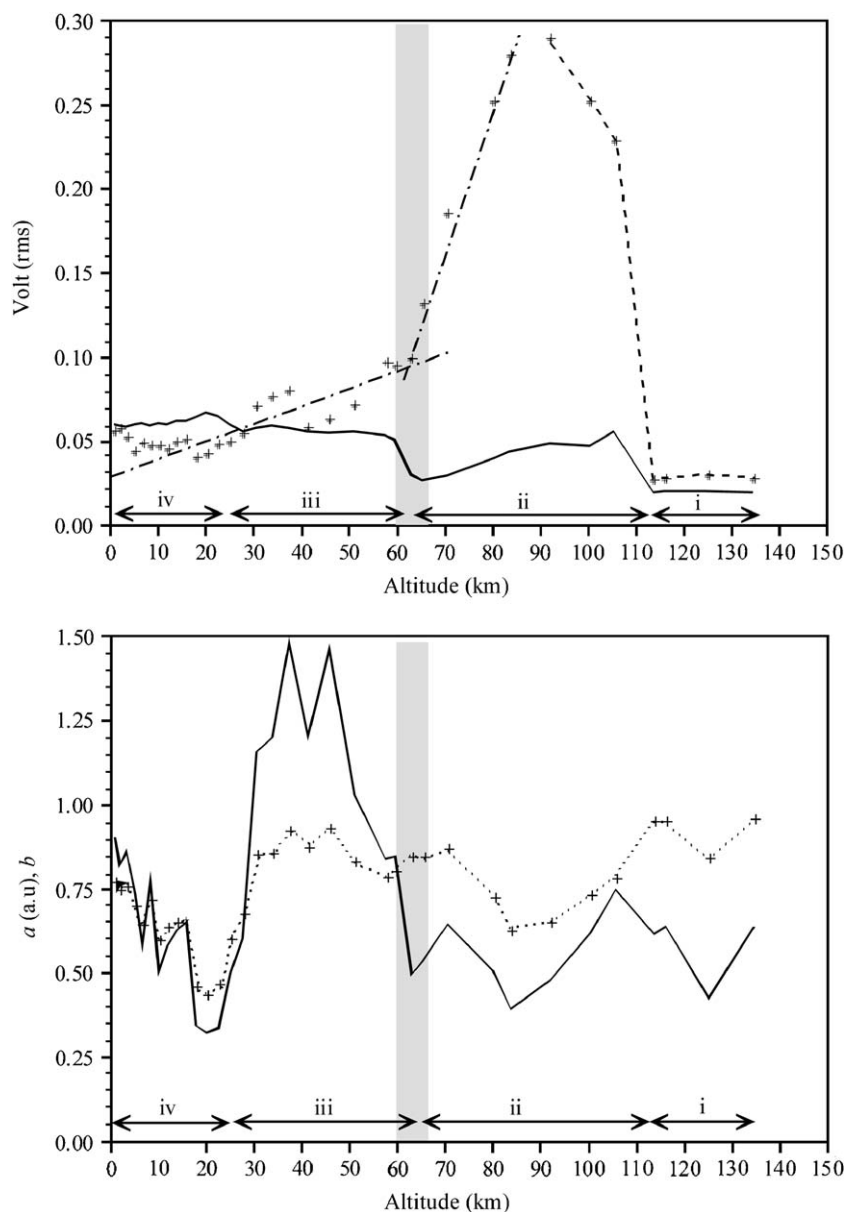

Fig. 1. Top panel: VADC amplitude profiles (see Section 2.1) of the extracted 36 Hz signal X (crosses for average values and dash-dot line for best fit), and broadband ELF component (solid line). The symbols i to iv are referring to portions defined in Section 2.2. The grey area around 62 km highlights the presence of the GCR layer. Bottom panel: altitude profiles of ELF noise spectrum parameters a (solid line) and b (crosses) fitting the law a/f^b.
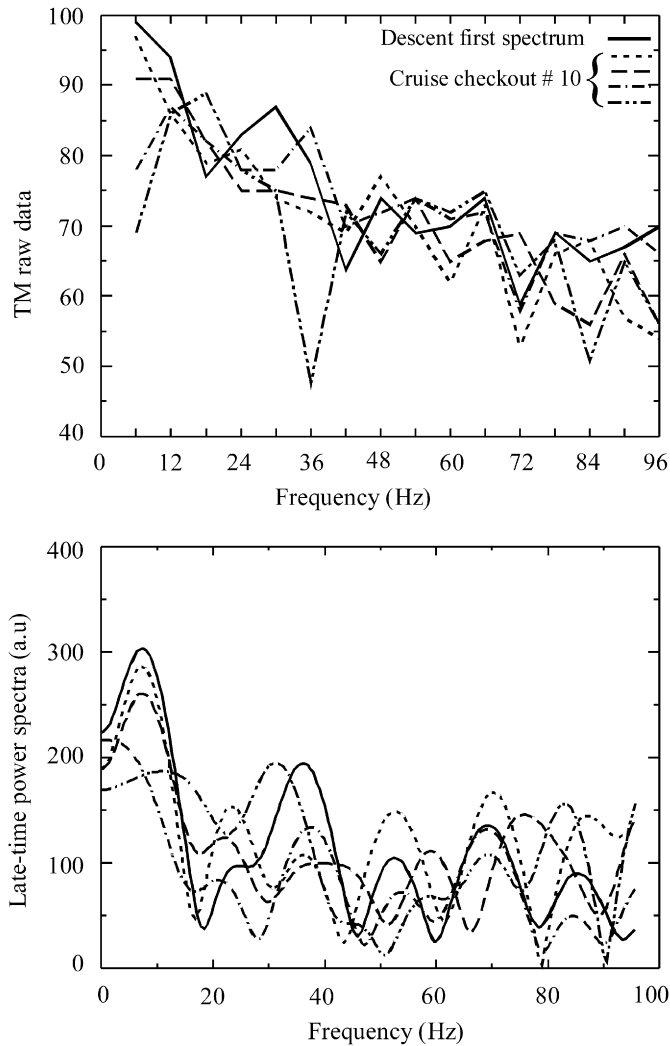
Fig. 2. Top panel: plots of ELF–PWA power spectra in Mode 1, as they appear in telemetry after 8 bits logarithmic compression (256 levels). The 16 spectral bins between 6 and 96 Hz have been interpolated here for the sake of clarity. Solid line: first spectrum obtained at 140 km, same as Fig. 5a in Morente et al. (2008). Discontinuous lines: first four spectra recorded during the cruise checkout #10, with the antenna stowed under the thermal cover. Bottom panel: corresponding responses derived from the late-time analysis. Again, the solid line corresponds to Fig. 5d in Morente et al. (2008).

are consistent with instrumental noise and do not represent "significant evidence of electrical activity in Titan's atmosphere" as claimed by Morente et al. (2008).

The abnormal behavior observed during the initial part of the descent is attributed to the fact that, at least one, possibly two booms were probably not locked properly into position until the main parachute was released at 110 km. A similar phenomenon is invoked to account for the inconsistent data of the mutual impedance experiment at the same time (Hamelin et al., 2007). Due to the poor reliability, we will discard the data of that portion in the subsequent analysis.

(ii) The second portion starts just after stabilization of the drogue parachute and stops with the pre-programmed change in the PWA mode (110–61 km, MT 912–1926 s). The end of this portion happens to coincide fortuitously with the crossing at around 60–70 km of the so-called GCR conductivity layer mentioned in the introduction. Immediately after drogue parachute deployment, which is assumed to have caused the nominal locking of the booms, we observe a very

strong increase of the signal X, with a maximum at around 92 km followed by a linear decay down to 64–65 km. The ELF noise level is always 5 or 6 times weaker than the signal X in this region, so we believe that the fitted ELF spectrum is disturbed by the high level of the signal, whose spectrum overlaps the bins around 36 Hz. Therefore, no particular attention will be given to the significance of the ELF noise in that portion.

(iii) The third portion extends from the PWA mode change and the maximum conductivity of the GCR layer around 62 km, until 26 km (MT 1930–4484 s), during which the smoothed level of the signal X continues to decrease with long-term variations up to 20% in amplitude around a continuous decay. The least square-fitted linear slope in this region is 8 times lower than that above 64 km. Such a sudden change of slope is proved to be independent of the PWA mode change. We show in Fig. 3 a zoomed plot of running mean values of the 36 Hz signal amplitude together with the values of the conductivity obtained by the MI experiment during this portion between 70 and 54 km. The average values of two data sets of 148 and 312 s duration, respectively, before and after the mode change (MT 1778–2242 s), decrease slightly from 0.095 to 0.093 V, without significant jump ($<$10%) of individual data points within time intervals of ± 4 s around the mode change (not visible at the scale of Fig. 3). In contrast, the ELF noise component, at the same time, increases suddenly from 0.031 to 0.051 V (Fig. 1, top panel), which is in rough agreement with the factor $\sqrt{2}$ corresponding to the increase of the DFT bandwidth. The broadband ELF noise spectrum shape is close to a/f, which suggests a thermal noise nature, with its origin not yet clearly identified.

(iv) The fourth portion is the final phase of the descent (26–0.7 km, MT 4486–8870 s), during which the ELF noise component becomes stronger than the signal X. At around 20 km, the noise strength increases slightly, but the spectrum clearly flattens more significantly towards a white-noise spectrum with b tending to 0.4 over a short distance (20 ± 2 km). Such feature indicates a natural source similar to aerosol shot-noise which was simulated during post-flight laboratory tests (Béghin et al., 2007). This is likely due to the presence of a thin haze layer detected indeed at 21 km by the Huygens camera (Tomasko et al., 2005).
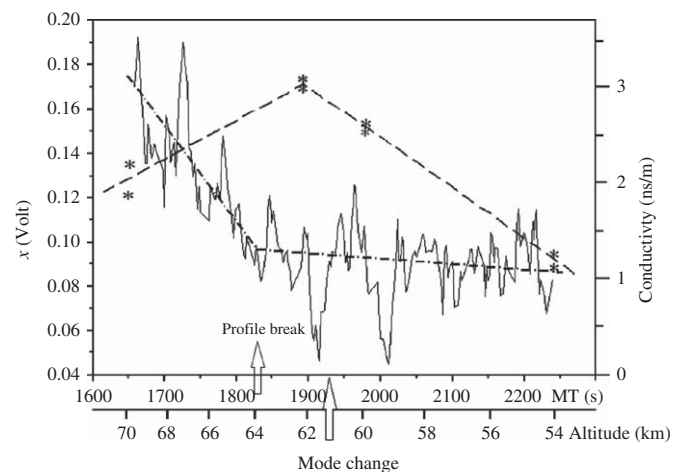

Fig. 3. Zoom of the amplitude profile of the 36 Hz signal while the Huygens Probe is crossing the GCR layer: solid line for sliding mean over 10 data points, dash-dot line for best fit as top panel in Fig. 1. Stars and interpolated dash lines are conductivity values obtained by the MI experiment (Hamelin et al., 2007). The pre-programmed change from Mode # 1 to # 2 occurred at 1930 s (see Section 2.1).

The most remarkable feature observed in the amplitude profile of the 36 Hz signal is obviously the break in the vertical gradient that occurs at ~64 km, around the maximum of conductivity of the GCR layer measured with a poorer altitude resolution than the ELF signal (Fig. 3). Unfortunately, the PWA mode change just happens to have occurred about 100 s (3 km) after the signal gradient break, as seen in Fig. 3. If both events were somehow related physically, one should have observed a sharp change in the 36 Hz signal amplitude exactly at the time of mode change instead of the break in the altitude profile. Even if some process could have modified the transfer function of the system for the 36 Hz signal, no explanation can be found indeed for a corresponding change in the vertical gradient of the signal amplitude. Thus, the gradient break at 62 km is a major indication that the observed 36 Hz signal must be a natural phenomenon influenced only by the local conductivity of the atmosphere. To confirm that the extracted signal X is a natural wave, we have used the Huygens Probe attitude data deduced by Karkoschka et al. (2007), from the DISR experiment and from the automatic gain control (AGC) of the Huygens–Cassini telemetry link.

3. Correlation of signal amplitude variations with Huygens Probe attitude

On Earth, the conventional methods for wave-direction finding are performed by using three-dimensional steady sensors (for VLF–ELF, see e.g., Hayakawa et al., 1981 and Labendz, 1998 for Schumann resonance). When such capability is not available in space experiments, the simplest way consists of taking advantage of the antenna rotation as a goniometric finder, like done sometimes for rocket-borne VLF measurements (e.g., Béghin, 1967). This method, that we have used here, implies that the field polarization may be assumed to remain quite stationary during a sufficient period of time compared to the spin period. From the three angular coordinates deduced from DISR experiment, we may define two variables necessary to account for the dynamical reception pattern of the antenna, i.e., the absolute azimuth of the dipole antenna, lying on the Huygens axis Yp, with respect to the East–West direction, and the tilt of the Huygens axis Xp (perpendicular to the instrument platform plane $Yp–Zp$), with respect to the local vertical (for details, see Fig. 2 in Fulchignoni et al., 2002). In addition to the regular dynamics of a spinning body, the Huygens Probe exhibits two swing modes around the parachute bridles (Karkoschka et al., 2007). Around and below 70 km, the fastest mode could have produced periods as short as one second, with particularly strong amplitudes. We have performed a first test to check if the procedure of variable separation between tilt and azimuth could be applicable. For that purpose, we tried to see whether the variations of the signal amplitude X were statistically correlated with the tilt inclosing slow swing components.

3.1. Tilt contribution

We have selected a set of 50 individual angular coordinates from Table 1 in Karkoschka et al. (2007), which correspond to the region of best signal-to-noise ratio of the 36 Hz signal, i.e., between 110 and 30 km. The majority of the values in that table can be associated with PWA measurements with a time shift $\delta t \sim \pm 1$ to 2 s with respect to the DISR frame. Since 2 s is the order of magnitude of the fast-swing mode, and corresponds to a spin rotation of 120° at 100 km and 30° at 30 km, we cannot know the exact attitude of the antenna corresponding to each PWA data point. One can however consider, as a working hypothesis, that the signal is a quasi-stationary wave, with a predominantly vertical electric field component throughout the descent, as on Earth in case of the Schumann Transverse Magnetic mode (e.g., Sentman, 1990). For these conditions, the amplitude of the horizontal component is assumed everywhere to be less than 10% of the vertical component (Simões et al., 2007). Therefore, by neglecting the modulation due to the horizontal component, the signal strength must be maximum, in average twice per rotation, at the moments when the angle between the antenna and the local vertical reaches its minimum value. This condition should occur when the tilt of the Huygens axis Xp is a maximum, and should be associated with two signal minima, viz., $\frac{1}{4}$ of a rotation before and after each maximum, when the antenna crosses the local horizontal plane. If θ is the average value of the tilt including fast swing during elapsed times of the order of δt at least, since the values of δt are assumed being randomly distributed, we show in Section 5.1 that the mean amplitude of the signal should have to be proportionally statistical to θ. Therefore, we ought to observe a linear correlation between the amplitude of the signal X and the tilt. The plot in Fig. 4 shows that is not the case. Thus, we must reject the hypothesis made above that a dominating vertical electric field component is present. We may consider now the azimuth variable independently from the tilt. We then proceed with a second hypothesis that a significant horizontal component exists. The latter will be assumed roughly polarized linearly, aligned perpendicularly to a preferential source direction, so as to
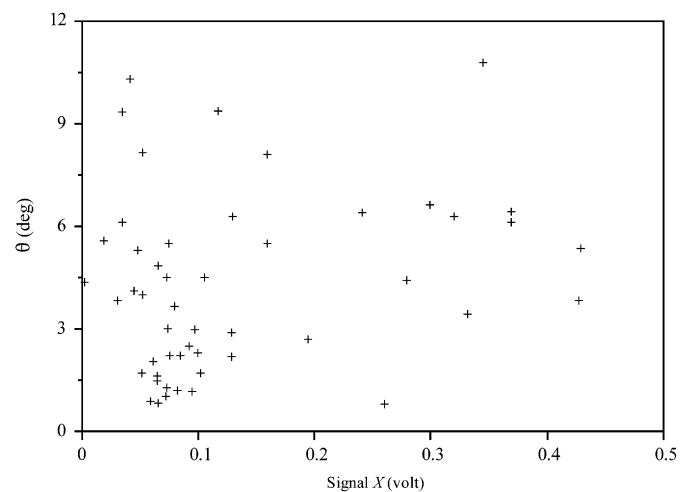

Fig. 4. Two-dimensional distribution of the signal X amplitude versus tilt of Huygens nominal spin axis Xp, for 50 PWA–DISR quasi-synchronous data points between 110 and 33 km.

Table 1
Average and probable extreme values of tilt and X for two samples of 11 DSRI-PWA joint measurements each, at around 77.8 km (MT 1409–1529 s) and 41.9 km (MT 2564–3093 s).

Mean altitude (km)	Average of $\underline{X}$ (mV)	Average of θ (deg)	Tilt standard deviation σ_θ (deg)	Maximum of $(\theta + \sigma_\theta)$ (deg)	Minimum of $(\theta - \sigma_\theta)$ (deg)
77.8	259	5.2	2.6	7.8	2.6
41.9	52.8	4.5	2.8	7.3	1.7

be detected by using the same principle as for goniometric wave-direction finding.

3.2. Azimuth contribution

In the following, we will use the conventional terminology and analytical methods for statistics (see e.g., Kendall and Stuart, 1969; Aïvazian, 1970; Scott, 1985). The azimuth data are from Table 3 in Karkoschka et al. (2007). The absolute origin of azimuth is such that the Huygens axis Zp lies within the north-zenith half plane, which is very close to the direction at which the DISR camera is looking northward. The azimuth angle denoted here by γ is measured clockwise positively, i.e., eastwards. In spite of significant fast variations in the rotation velocity, each interval of 10 s as processed by Karkoschka et al. (2007) makes it possible to use linear interpolation to provide a precision of 1° or 2° most of the time, which is more than sufficient for the following statistical analysis. We have built a file with azimuth values corresponding to each of the PWA data points. However, the irregular and relatively slow sampling rate of PWA data, in the second mode of operation, i.e., by sets of 9 data points with 2 s intervals repeatedly every 64 s, does not make it possible to treat correctly sequences for which the spin period is shorter than 15 s. Otherwise, one would get less than 8 PWA data points per rotation, which would reduce accordingly the accuracy of our investigation. This constraint obliged us to limit the study to altitudes below about 55 km, where the spin period oversteps satisfactorily the above limit. By chance, this altitude range coincides with the region of highest accuracy of the azimuth data derived primarily from the AGC of the Huygens–Cassini link, which becomes increasingly periodic (Karkoschka et al., 2007). In the lower part of the descent, the average amplitude of signal X becomes smaller than the ELF noise (Fig. 1), so we will discard here the region below 28 km, because we want to preserve an acceptable signal-to-noise ratio. Furthermore, to reveal the expected correlation between the signal amplitude and the azimuth more easily, we will use normalized signal amplitudes with respect to an average value computed over a few rotations.

Over a relatively wide altitude range (55–28 km), which corresponds roughly to portion (iii), the average level of the signal varies by a factor ~1.8. But we observe short-term variations (<4 s), not shown in Fig. 1, which in some instances are larger than the running mean in that region. To avoid a strong influence of variations slower than a few spin periods, we use the conventional procedure of levelling (sometimes called weighting). Such a procedure is necessary when the sample comprises several independent parameters, as is the case here with the tilt, the azimuth and the long-term variations of the signal. Regarding the tilt, although this parameter seems to have insignificant influence according to the conclusion of Section 3.1, we cannot exclude the possibility that it could be somewhat related to fast variations of the rotation velocity. In any case, one may reduce to two the number of independent parameters, viz., the azimuth, whether or not it is linked to the tilt, including the swing, and the long-term natural variations which are altitude dependant. The altitude profile of the long-term smoothed variations is known from the plot in Fig. 1.

We started by first surveying some subsets of 45 data points within the region (iii) to identify any general feature appearing systematically in the signal amplitude distribution versus the azimuth. For that purpose we produced histograms, within 6 classes of azimuth distributed between 0° and 360°, of occurrence (i.e., frequency) of the number of points when the signal amplitude exceeds the average of the given subset. In the example plotted in Fig. 5 one can see a bimodal distribution at 0–60° and
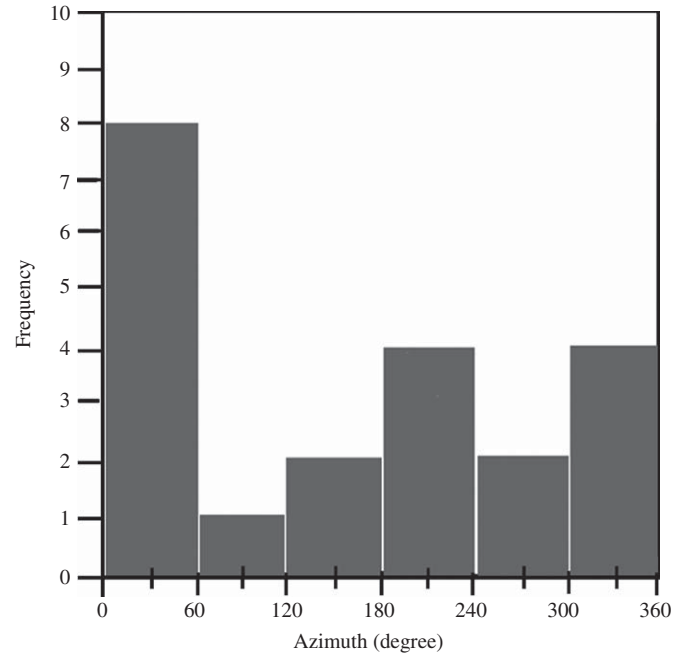

Fig. 5. Occurrence distribution of the number of X values whose amplitude is larger than their local mean within 6 azimuth classes, for one sample of 45 data points at around 42 km (MT 2956–3096 s).

180–240°, as a clear indication of a modulation twice per spin period. However, in the first part of the region (iii) from 55 to 44 km, we have observed a large dispersion of those modes which is interpreted as due to sources not being really stationary (see Section 4). Finally, we have selected a sample of a total duration of 19 min 10 s below the altitude where the phenomenon appears reasonably stationary. The sample contains 360 individual power spectra, from about 45 to 30 km (MT from 2792 to 3942 s), comprising 8 subsets with subscript j, of about 140 s duration each, containing 45 values with subscript i, so as to be compatible with the spin period (15–35 s). This ensures at least 4 rotations per subset. From one subset to the next, the average amplitude of the long-term variations may have changed, so we define the local mean value as the following:

$$\underline{X}_j = \frac{1}{45} \sum_{i=1}^{45} X_{j,i} \quad \text{and} \quad \frac{1}{45} \sum_{i=1}^{45} (X_{i,j}/\underline{X}_j) = \frac{1}{360} \sum_{j=1}^{8} \sum_{i=1}^{45} (X_{i,j}/\underline{X}_j) = 1$$

(3)

where $X_{i,j}$ is the extracted signal amplitude as defined by Eq. (2) with the running subscripts i and j, and $\underline{X}_j$ the local mean value of subset j. In the following, all data points $X_{i,j}$ are normalized with respect to $\underline{X}_j$ using $x_{i,j} = X_{i,j}/\underline{X}_j$. Thanks to the weighting procedure, the dynamic range of normalized amplitudes is significantly reduced since only 6 out of 360 data points are beyond twice their standard mean ($x_{i,j} > 2$) and none beyond 2.5 times. According to the usual rule for short samples (Kendall and Stuart, 1969), the optimal number of classes for a sample containing 360 data points would be 10, but because the sharp decrease of the distribution above $x = 2$, we may keep 10 classes from 0 to 2 and two complementary classes for $2 < x < 3$.

The distribution of normalized signal amplitudes x, as plotted in Fig. 6, exhibits positive skewness, i.e., an asymmetry compared to the normal distribution. We attribute this phenomenon to the detection threshold for weaker signals. If the original signal is supposed to obey a normal distribution, the true average value $\underline{X}_j$ and the median (Q_2) must be identical. Because of the antenna-receiver sensitivity and/or the presence of ELF noise, all the weak

values are lost and kept the threshold value. Consequently, the apparent mean of the subset sample increases. On the other hand, there is always the same proportion of real signal amplitudes distributed in equal parts (50%) on both sides of the median, which retains the value of the true mean. Therefore, a positive skew appears in the observed distribution, as seen in Fig. 6 by a left-hand-side shift of the median and other quartiles with respect to the apparent mean. We have checked that the moments of higher order such as the kurtosis lie within the limits of a normal distribution.

3.3. Two-dimensional analysis of spin modulation

After these preliminary analyses, we may proceed with the two-dimensional statistical analysis of the selected sample by considering instead the individual amplitude distributions within

Fig. 6. Distribution of the normalized signal x amplitude for the selected sample between 45 and 30 km. Note the positive skewness emphasized by left-hand-side shift of the three quartiles Q_1, Q_2 and Q_3. The normalized standard deviation is $\sigma = 0.45$.

each class of azimuth. Taking into account the available number of data points ($N = 360$), keeping again 6 azimuth classes of $60°$ width each, we get 56–65 values per class, depending on the way they are distributed in time. The conventional optimum would be 7 classes of amplitude for each of the 6 azimuth classes. Since we have only 6 data points such as $x > 2$, one can take 6 classes from $x = 0$ to 2 with a regular width $\Delta = 1/3$, plus one complementary class for $x > 2$. As for Fig. 5, we performed a first test by centering arbitrarily the first azimuth class at $\gamma_0 = 30°$ ($0 \leqslant \gamma < 60°$). The results are plotted in the form of 6 histograms in Fig. 7. In each class, we note the frequency of values such as $x > 1$. It is important to point out that the mean value in each class of azimuth is here no longer equal to 1. This new mean value is different indeed from the mean of $X_{i,j}/\underline{X}_j$ values, since within the same class of azimuth, we are considering normalized amplitudes of points coming from different regions. A major advantage of this procedure is to increase the confidence level of the statistical results, since the random repartition of data during more than 19 min increases the probability of emphasizing the spin modulation of the signal, independently of time of flight.

One can already anticipate that the difference in occurrence between large and small values, as seen in Fig. 7, i.e., 60% above the average lying in the range 0–60° against 40% in the range 180–240°, is a good indication of a real spin modulation. We propose, however, to quantify more accurately the degree of correlation between the signal amplitude $x(t)$ and a periodic statistical function $F(\gamma)$. The initial phase of this function should not depend on the arbitrary choice of the lower limit of the first class of azimuth. In the first test, we took $\gamma_0 = 0°$ as the lower boundary for the class 0–60°. If the spin modulation function $F_1(\gamma)$ obtained with test #1 does not result from a stochastic process, we must recover a quite similar function with a second test, by shifting the origin of classes γ_0 by $(C+\eta)\,60°$, where C is an integer and $|\eta| < 1$. Such a procedure is in fact an estimator of the second order, where $|\eta|$ is not necessarily quantified, known as averaged shifted histogram (ASH) and developed by Rice University (Scott, 1985) for the processing of LANDSAT IV satellite data. The change of C would not obviously produce any effect since it would simply result in permuting the existing classes. Only fractional displacement would be significant. Therefore, in test #2 we move the
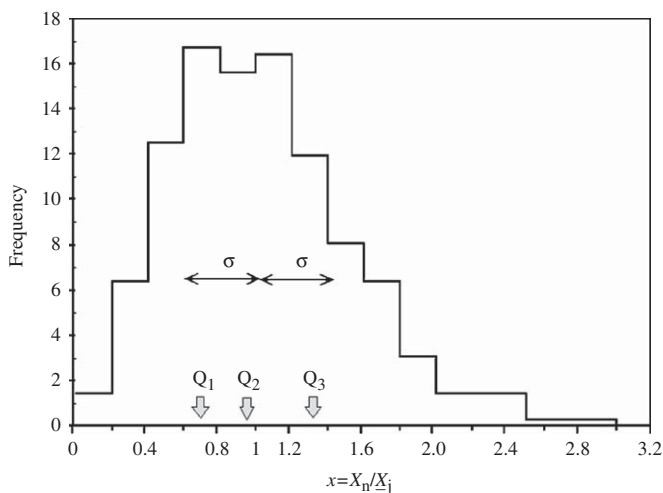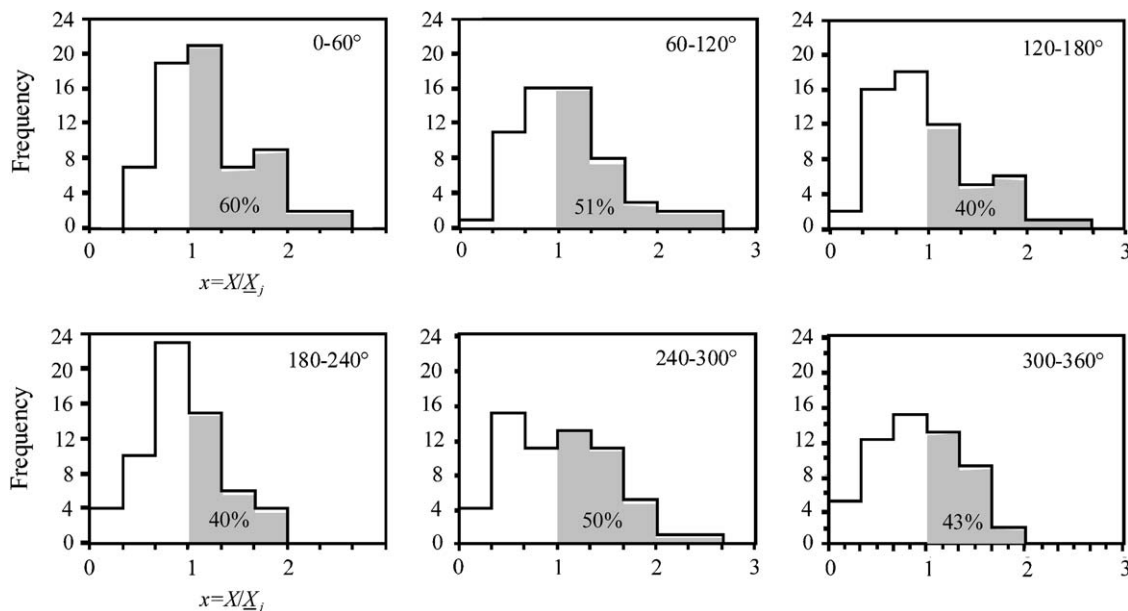

Fig. 7. Two-dimensional amplitude distributions of signal x within 6 classes of azimuth, for the selected sample between 45 and 30 km (test #1). The grey areas highlight the percentage of values $x_{i,j}$ which exceed the mean $\underline{X}_j$ within their own subset j.

lower limits of our 6 classes 30° towards the left ($\eta = -0.5$), so $\gamma_0 = 330°$, which put the central value of the first class at the azimuth $\gamma = 0$. By doing so, we redistribute randomly about 50% of new data points in each class of azimuth. The resulting spin modulation function $F(\gamma)$ arising from the two tests, and the associated statistical parameters, are plotted in Figs. 8 and 9, respectively.

We clearly see two maxima per rotation, lying, respectively, at around 30–60° and 240–270°, and two minima at around 0° and 180°. The difference between maximum and minimum values is that 60% of large amplitude signals are observed in one direction, compared to only 40% after further rotation by 110–120°. However, surprisingly, the two maxima exhibit quite different
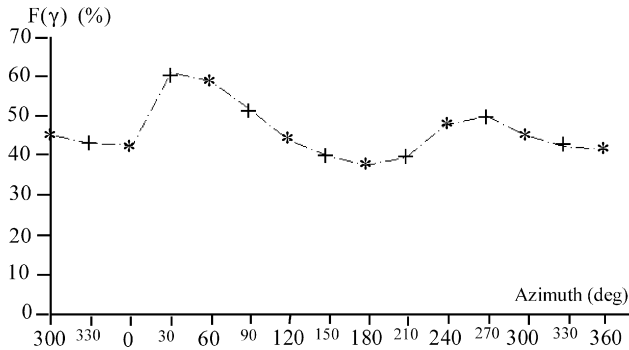

Fig. 8. Averaged Shifted Histogram (ASH, see Section 3.3) of the spin modulation function $F(\gamma)$, in terms of percentage of values overlapping the average value ($x > 1$) for test #1 with $\gamma_0 = 0$ (crosses) and test #2 with $\gamma_0 = 330°$ (stars).

amplitudes, contrary to what would be expected after just half a rotation of a perfectly symmetrical dipole. This phenomenon is not yet totally understood, but the more likely interpretation involves the particular design of booms and electronics. There is indeed a double asymmetry, first, of the positioning of the Relaxation Probe sensors with respect to the MI receiving sensors, and second, of the RP grounding circuitry (see Fig. 2 in Fulchignoni et al., 2002 and Grard et al., 2006). Therefore, in the presence of a horizontal drift of the gondola, the wake of the RP disks might affect differently the interfering contribution on the 36 Hz signal due to the induced ELF noise, as proved by shot-noise generation when spraying aerosols around the sensors (Béghin et al., 2007). Nevertheless, the reality and coherence of the modulation are confirmed by the behavior of the statistical parameters such as quartiles, average, mode, skewness and kurtosis which are plotted in Fig. 9. Apart from the kurtosis variations (Fig. 9d), which are not significant, since they lie within the area of a random distribution, according to the standard criterion for samples of about 60 data points in each azimuth class (e.g., Kendall and Stuart, 1969), all other coefficients exhibit the spin modulation of twice the rotation rate. Moreover, the behavior of skewness (Fig. 9c) corresponds satisfactorily to the positive skew which is attributed to the detection threshold for low values in the total sample, as observed in Fig. 6. Indeed, the skewness rises above the region of normality (grey area) when the median is lower than the average of the set. However, this occurs essentially for values of azimuth lying around 0° and 150°, when Q_3 is minimum, i.e., when 75% of values are such as $x < 1.15$. Thus, there is a strong proportion of weak signals. Reciprocally, when the distribution is not biased (grey area) for azimuths around 60–90° and 240–270°, there is a
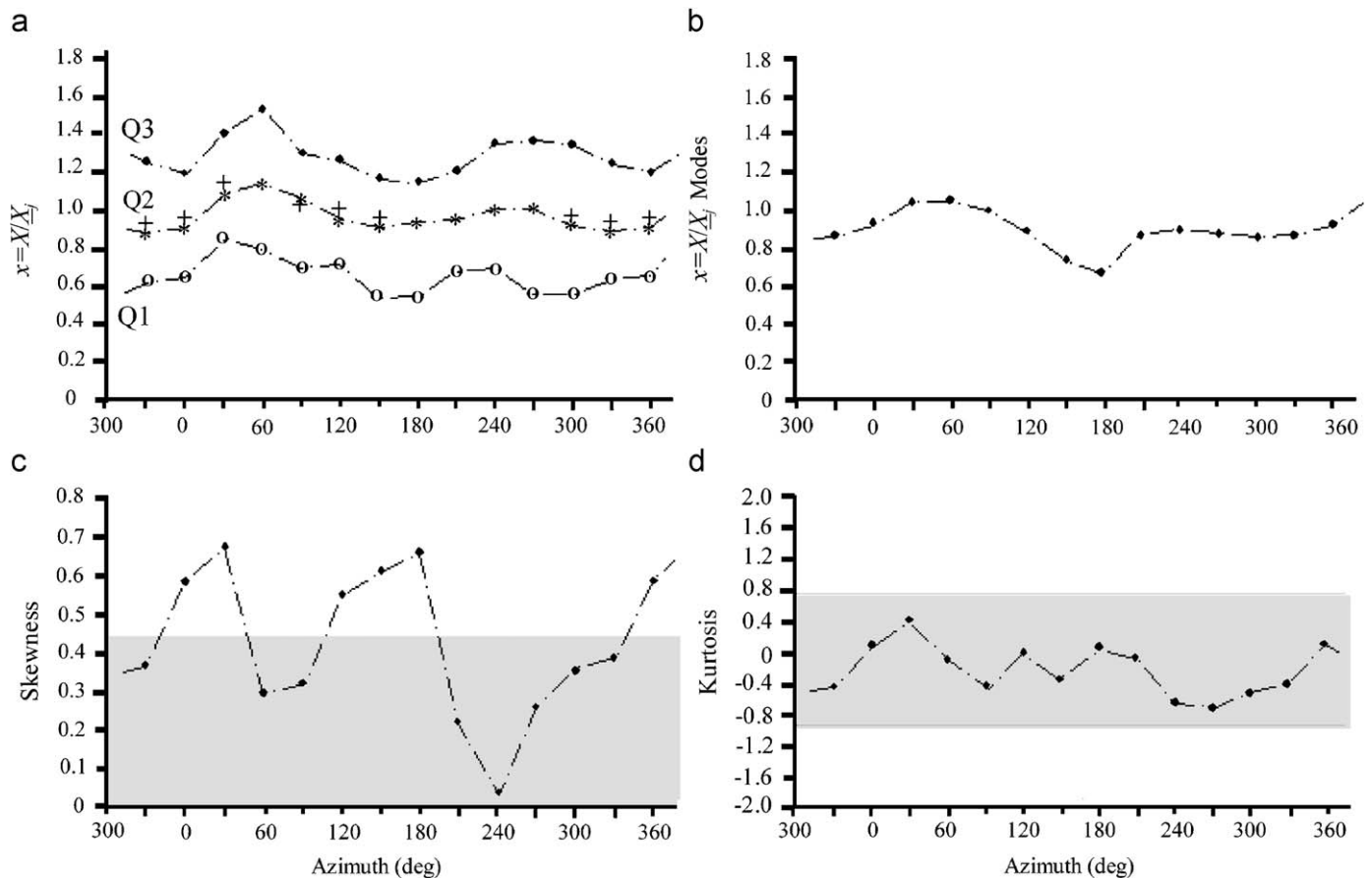

Fig. 9. Statistical parameters of the ASH function $F(\gamma)$ plotted in Fig. 8, for tests #1 and #2. Panel (a): the three quartiles and the mean value (crosses) whenever it differs from Q_2 by more than 2%. Panel (b): mode positions. Panels (c) and (d): skewness and kurtosis, grey surfaces are areas of normality.

greater proportion of strong signals, with $Q_2 > 1$, which leads to a diminution of the threshold effect.

We give in Appendix A the method used for evaluating the regression coefficient between the data sample and the modulation function, and the associated confidence level as well. One finds that if we had proceeded with an infinite number of tests, by assuming the same distribution of random noise over a much longer sample (N tending to infinity), the value of the correlation ratio would lie between 7% and 27% with a confidence level of 95%. Thus, the derived modulation function plotted in Fig. 8 is significant with 95% probability. Knowing the relatively poor quality of our data, a mean correlation ratio of 17% seems reasonably consistent with natural signals, which are fluctuating both in amplitude and azimuth. Such variability is indeed quite similar to direction findings of Earth's Schumann resonance, as a function of azimuth and local time of the lightning sources (Labendz, 1998; Belyaev et al., 1999). Therefore, we accept the hypothesis that the observed signal at 36 Hz is consistent with incoming polarized electromagnetic waves. Since the PWA antenna is perpendicular to the Huygens azimuth reference axis Zp, we interpret our observation of preferential polarization directions as due to the presence of localized source areas, clustered on geographical headings of 30–60° East and/or 90–110° West.

4. Source location and injection mechanism

4.1. Data from Titan Cassini flybys

Several Titan flybys have been performed by the Cassini Saturn orbiter since 2004. We are particularly interested in data obtained from the magnetometer (MAG) (Dougherty et al., 2004) and from the plasma wave package RPWS (Gurnett et al., 2004). The measurements obtained by the first instrument allow us to localize the regions where the tail currents are connected to Titan's upper ionosphere, with the magnetic lines of force draped around the ram hemisphere of the moon. The second instrument helps identifying the ELF emissions that we suppose to be the source of the Huygens 36 Hz signal. The magnetometer measures three components of the dc magnetic field, in a reference frame centered on Titan, aligned according to Saturn's magnetic dipole and the direction of the Kronian nominal co-rotating plasma. From the numerous flybys through Titan's wake, a few case studies have been analyzed to date (e.g., Neubauer et al., 2006; Wahlund et al., 2005; Agren et al., 2007; Bertucci et al., 2007 and Bertucci et al., 2008; Modolo et al., 2007), confirming, but with better resolution, a preliminary model of the moon's interaction with Saturn's magnetosphere which was derived from Voyager observations (e.g., Hartle et al., 1982; Gurnett et al., 1982; review by Blanc et al., 2002). We will concentrate our attention here on one particular encounter over Titan's northern polar region which occurred on April 16, 2005 (T5 flyby).

We retained this flyby, not only for the interest of crossing the interaction region on ram-side of the polar cap, but also because it is one of the deepest incursions within the ionosphere, with the closest approach (CA) altitude of 1050 km occurring at around 19:12 UT. In Fig. 10, we show the three-dimensional evolution of the magnetic field vector plotted along the Cassini trajectory, superposed on a sketch of Titan's wake when it would be, ideally, opposite to Saturn's co-rotating plasma flow. Outside the magnetotail, the undisturbed Kronian magnetic field is pointing south, as expected, but with a quite unusually large tilt angle (~65°) toward both the directions of Saturn's and that of Titan's tail. This tilt is due to the fact that at the time of the encounter, Titan is lying south of Saturn's-warped magnetodisk in the dawn
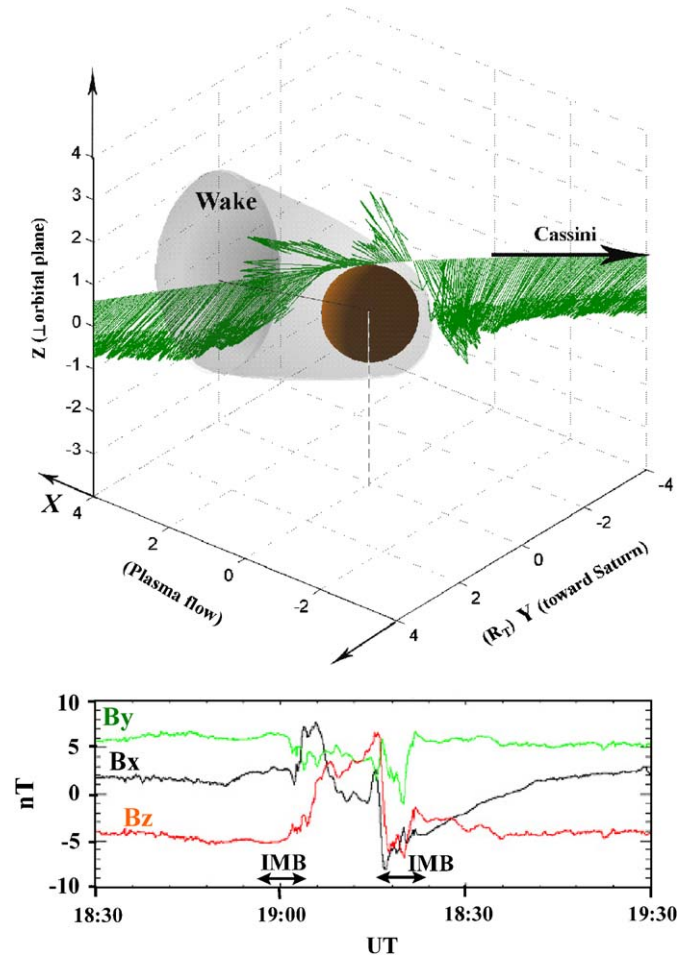

Fig. 10. Top panel: three-dimensional plot of the magnetic field vector along the Cassini trajectory above the Titan's northern polar cap of T5 flyby, on April 16, 2005. Bottom panel: amplitude of the three components The estimated crossings of the induced magnetospheric boundary (IMB) are shown at around 19.02 and 19.20 UT, respectively, on both sides of the closest approach (CA) about 1050 km from the surface.

sector, where the magnetic field is strongly stretched and swept back with respect to co-rotation (Bertucci et al., 2009). The particular point of interest here is the signature of the inbound and outbound crossings of the induced magnetospheric boundary (IMB), visible in the plot of the three components of the magnetic field in bottom panel of Fig. 10, at around 19:02 and 19:20 UT, respectively. This boundary is also referred as magnetic pileup, or draping boundary (e.g., Neubauer et al., 2006), since it is thought to point out the regions where the field lines are strongly draped. Below about 1400 km, collisions are responsible for the dissipation of the induced magnetotail and magnetospheric currents, and usually the magnetic field falls-off near CA. The situation is quite different during the T5 encounter here, as the field strength around CA is about 4.7 nT, with an unusual vertical component. We believe that the low-altitude fields have penetrated down, without being damped due to the fact that the flow from Saturn is impinging on the night side, where charged particle densities are small and the field diffuses without being attenuated. The sign reversal of the B_x component around CA, clearly visible on Fig. 10, indicates indeed that the orbiter was exploring both lobes of Titan's induced magnetosphere between the two IMB crossings. The fast rotations in the magnetic field vector at each crossing, confirmed by the minimum variance analyses of the field strength, are interpreted as signatures of

strong currents flowing at the boundaries. Therefore, we believe such currents are parts of ionospheric branches closing the global magnetotail circuitry, involving a global current estimated over 10^5 A (Béghin et al., 2007).

In the latter paper, the authors invoked the ELF emissions driven by energy dissipation of such induced currents, as a possible source for the Titan's Schumann-like resonance. The generation mechanism was assumed to involve the ion-acoustic turbulence, possibly coupled to the electromagnetic whistler mode. The latter is the right-hand-polarized ordinary mode in a magnetized plasma (see e.g., Booker, 1984). Such ELF waves, from a few Hz up to 1 kHz, were observed when Voyager 1 was crossing the two external boundaries of the far magnetotail and were identified as sheath noise by analogy with Earth's magnetosphere (Gurnett et al., 1982). During the Titan's flybys by Cassini, and especially near the closest approach such as during T5, the orbiter active attitude control system and several other instruments may induce interferences which make it quite difficult to discriminate natural waves from instrumental artifacts. Nevertheless, the interface regions between the magnetotail plasma and the ionosphere are the subject of intensive investigations, and a few preliminary case studies have been published (e.g., Modolo et al., 2007). Although the generation mechanism of ELF waves in these regions, and the exact location of the sources, are not yet perfectly identified in spite of several tens of Titan flybys, we have however confirmation of the quasi-permanent presence of ELF electrostatic and/or electromagnetic emissions in each lobe crossing.

We show in Fig. 11 the color spectrogram of the five ELF components (two electric and three magnetic) obtained with the RPWS experiment during the same T5 encounter as above. Some gaps of data lost have been removed here (black portions), and several doubtful strong bursts are hidden, such as those occurring for instance at around 18:53–18:55 UT, because they are thought to be related to the Langmuir Probe operating modes (Hospodarsky, University of Iowa, private communication, 2008). In spite of those experimental constraints, the events that occur around the inbound crossing of the Saturn-side IMB (marked on bottom of Fig. 11, at 19:02 UT$\pm$2 min), and the opposite one (at 19:20 UT$\pm$2 min), appear however to be credible wave features. Unlike most of far-wake flybys, where the signature of electromagnetic waves is visible on both electric and magnetic components, while Cassini is crossing the external lobes of the magnetotail, no such behavior can be seen unambiguously here. One can remark indeed on the spectrograms in Fig. 11 that the probable natural wave features in vicinity of each IMB crossing is visible essentially on both electric components, as an indication of a nearby source region of electrostatic emissions. Moreover, we may notice that spectral components below 50 Hz are always present in each event.

4.2. Injection mechanism

In far-wake and upper ionospheric regions, where different kinds of electromagnetic emissions are supposed to be generated, the propagation of ELF waves is governed by the static magnetic field $\boldsymbol{B_0}$ in the whistler mode, and that is only possible for frequencies lower than the electron–cyclotron frequency f_{ce} and larger than the electron-neutral collision frequency v. The refractive index for the wave vector quasi-parallel to $\boldsymbol{B_0}$ in a collisional plasma (Booker, 1984, Section 13.2) is given by

$$n^2 = 1 - \frac{\chi}{1 - Y - jZ} \quad \text{with } \chi = \frac{\omega_p^2}{\omega^2};\ Y = \frac{\omega_{ce}}{\omega};\ Z = \frac{v}{\omega} \tag{4}$$

where ω_p, ω_{ce} and v are the angular plasma, cyclotron and collision frequencies, respectively. The electron-neutral collision

frequency is related to the electron mobility coefficient μ_e, and to the electron conductivity σ_e by the following relations:

$$v = \frac{q_e}{m_e \mu_e} = \frac{\varepsilon_0 \omega_p^2}{\sigma_e} = 2.84 \times 10^{-8} \frac{n_e}{\sigma_e} \text{ (SI units)} \tag{5}$$

where q_e and m_e are the electron charge and mass, respectively, and n_e the electron density.

For backward propagation deeper in the ionosphere, the refractive index is still governed by the magnetic field as long as $v < \omega_{ce}$, otherwise the scalar conductivity σ_e becomes dominant and the wave is progressively damped. We may anticipate that the transition altitude should lie well below 1000 km, at a level probably not accessible to in-situ measurements during Cassini flybys, in spite of the hope of reaching as low altitudes as 900 km at some point during the extended mission. In the case study shown in Figs. 10 and 11, the minimum magnetic field strength at 1050 km from the surface is 4.7 nT, which corresponds to $f_{ce} \sim 130$ Hz and the maximum electron density n_e at this altitude is of the order of 10^9 m^{-3} (Agren et al., 2007). No model specifies more than about 1 nT as the order of magnitude of field strength at the Titan surface, coming either from a hypothetical intrinsic internal source or from external origin. Because the field observed inside the ionosphere is mainly induced by current sheets, one can assume a roughly linear vertical profile, which leads to a value of ~ 2 nT, i.e., $f_{ce} \sim 56$ Hz, at least down to about 400 km. Therefore, the limit of f_{ce} would probably not be a problem preventing parent whistler waves at around 36 Hz reaching such low altitudes in a collisionless medium. However, according to Eqs. (4) and (5), the lower altitude transition between magnetized and collisional plasma for $f_{ce} = 50$ Hz occurs for an electron mobility $\mu_e \sim 5.6 \times 10^8$ m^2 V^{-1} s^{-1}. In these regions, this quantity may be deduced from the neutral density and temperature using the following expression (Banks and Kockarts, 1973):

$$\mu_e = q_e(2.33 \times 10^{-17} N_n T m_e)^{-1} \text{ (SI units)} \tag{6}$$

where N_n is the neutral density and T the temperature of the thermalized medium.

The physical atmospheric parameters such as mass density and temperature below 1500 km, derived from HASI during the entry phase until landing, allow us to estimate a vertical profile of the electron mobility. At 400 km, the mass density is $\sim 2 \times 10^{-5}$ kg m^{-3} and $T \sim 165$ K (Fulchignoni et al., 2005). Considering that nitrogen represents 95–97% of neutral gas, we get $N_n \sim 4 \times 10^{20}$ m^{-3}. Substituting these values in Eq. (6) we get an electron mobility $\mu_e \sim 10^5$ m^2 V^{-1} s^{-1}, which leads to a collision frequency more than three orders of magnitude greater than ω_{ce} around 400 km. A similar estimate using the vertical profile of mass density and temperature from Fulchignoni et al. (2005), leads to a transition altitude of about 800 km for $Z \approx 1$ at 36 Hz ($N_n \sim 6 \times 10^{16}$ m^{-3}, $T \sim 160$ K). In this region, the high electron density such as χ is much larger than one in Eq. (4), therefore, the imaginary part of the refractive index is much larger than one, so the medium behaves like a pure isotropic conductor, and the electromagnetic field could penetrate only a skin depth given by the usual equation

$$\delta = \left(\frac{2}{\mu_0 \omega \sigma_e}\right)^{1/2} \tag{7}$$

where μ_0 is the free-space permeability.

With an electron conductivity of the order of 10^{-2} S m^{-1} at 800 km (Simões et al., 2007), one gets a skin depth less than 1 km which does not allow the whistler-wave components to penetrate more deeply in the ionosphere. We must, thus, consider instead a direct generation mechanism of ion-acoustic turbulence in the ionosphere, and its consecutive coupling to isotropic
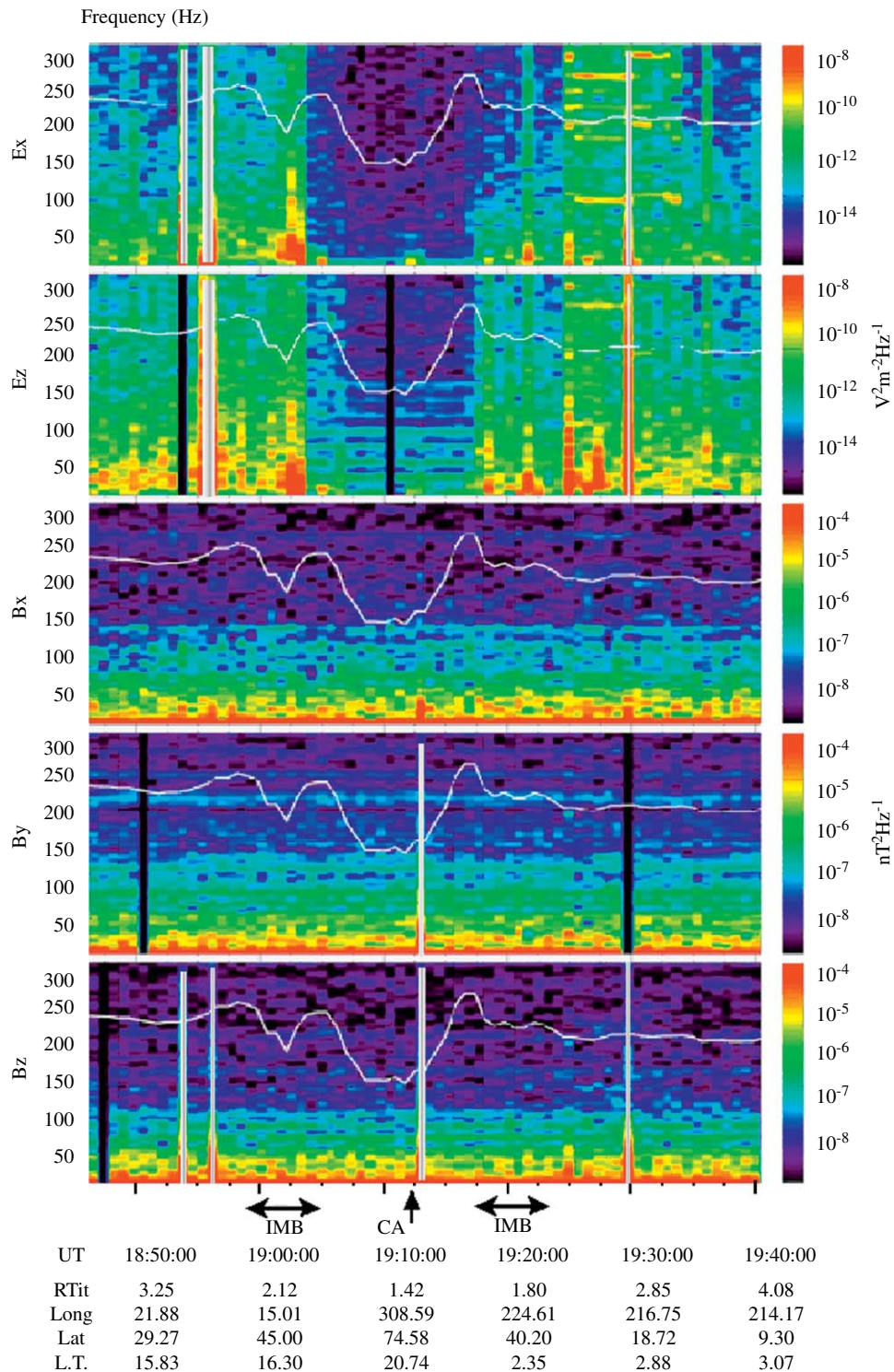
Fig. 11. RPWS spectrogram of 2 electric and 3 magnetic ELF components for the T5 flyby as in Fig. 10. The superimposed white line is the electron–cyclotron frequency f_{ce}. Black and hidden portions are gaps of data lost and probable instrumental interferences.

electromagnetic field through a parametric instability (e.g., Swanson, 1989). As in the case of the whistler mode in collisionless plasma, an ES–EM coupling is possible if the divergence of the combined electric fields is not zero. This condition may be satisfied within unmagnetized collisional plasma as well, since the Maxwell equation for div E includes a term of space-charge perturbation coming from the charge imbalance occurring with the ion-acoustic instability (Swanson,

1989). Moreover, several studies (e.g., Bychenkov et al., 1994; Merlino, 1997) show that the generation and the propagation of current-driven ion-acoustic waves are possible in unmagnetized collisional plasmas, such as we anticipate to be the case in Titan's lower ionosphere. Moreover, the instability could be scattered in the form of solitons (Shukla, 1986). One recalls that the major condition for generation of such emissions is that the relative electron–ion velocity V_{ei} be larger than the ion-acoustic

velocity v_{is}, i.e.,

$$V_{ei} > v_{is} \quad \text{with } v_{is} = \sqrt{\frac{K(T_e + 3T_i)}{m_i}} \tag{8}$$

where K is the Boltzmann's constant and m_i the ion mass. Between 1000 and 250 km, assuming a thermalized plasma containing essential nitrogen ions with a temperature of about 170 K (Fulchignoni et al., 2005), we get $v_{is} \sim 450 \, \text{m s}^{-1}$. In that region, the current density simply obeys the generalized Ohm's law ($J = \sigma_e E$) and the electron–ion drift velocity is given by

$$V_{ei} = \mu_e E = \frac{\sigma_e E}{n_e q_e} \tag{9}$$

With an induced dc electric field of the order of 1–$2 \, \text{mV m}^{-1}$, which is generally assumed for accelerating the pick-up ions from the ionosphere (e.g., Agren et al., 2007), an electron mobility of a few $10^5 \, \text{m}^2 \, \text{V}^{-1} \, \text{s}^{-1}$ would be sufficient for triggering the instability. This value is of the order of magnitude that we obtained from the neutral pressure measurements by HASI at around 400 km. Independently of the above estimate, if we consider the models between 250 and 400 km (Molina-Cuberos et al., 2004; Borucki et al., 2006; Simões et al., 2007), the values of electron conductivity and density in this region range between $\sigma_e \sim 10^{-5}$–$10^{-6} \, \text{S m}^{-1}$ and $n_e \sim 10^6$–$10^7 \, \text{m}^{-3}$, respectively, so the electron mobility is always larger than $10^5 \, \text{m}^2 \, \text{V}^{-1} \, \text{s}^{-1}$. Therefore, in a wide region below the ionopause, defined as the ionospheric boundary where the thermal pressure overlaps the magnetospheric pressure, the conditions for triggering the ion-acoustic instability are most likely satisfied down to $\sim 200 \, \text{km}$. This region is thus a convenient place for a direct generation, and therefore injection into the atmosphere of strong ELF electric fields with saturation amplitudes of the order of a few $\text{mV m}^{-1} \, \text{Hz}^{-1/2}$ (Béghin et al., 2007), which are found to be consistent with that of the Huygens 36 Hz signal.

5. Model of Titan's Schumann-like resonance

5.1. Conventional TM/TE modes

Although we dismissed in Section 3.1 the hypothesis of a major contribution of a vertical electric component, always associated with the conventional TM mode, we must consider nevertheless the hypothesis that there exists some combination of both TM and TE modes. To assess the validity of this hypothesis, we will consider here the altitude range 40–80 km, where the signal-to-noise ratio is good enough. Since we are dealing only with the electric field, we may have one vertical component E_V independent of the orientation of the $\boldsymbol{k}$ vector, plus two perpendicular horizontal components coming from both modes, leading to an elliptically polarized vector $\boldsymbol{E}_H$, with its largest axis dependant on k-direction. However, the relatively small modulation factor ($\pm 10\%$) observed in Fig. 8, plus the expected variability of the source direction, suggest a small eccentricity. So, we may consider the worst case of a quasi-circular polarization. Therefore, the modulation would come essentially from the contribution of $\boldsymbol{E}_V$. The rms voltage drop of the 36 Hz signal through the antenna, versus time t, is then given by the following relation:

$$V(t) = \frac{X}{G_{36}} = L_{eff}(\boldsymbol{E}_H \cos \alpha(t) + E_V |\sin \alpha(t)|)$$
$$\text{with } \alpha(t) = \underline{\theta}(t) \sin(\omega_s t - \gamma_0) \tag{10}$$

where $G_{36} = 13.5$, i.e. 22.6 dB (Jernej and Falkner, 2004), is the gain at 36 Hz of the analog system between the antenna and the input of the analog–digital converter; L_{eff} is the effective length of

the antenna (estimate $\sim 1.6 \, \text{m}$), E_H and E_V are the rms amplitudes of horizontal and vertical components, respectively, $\alpha(t)$ is the angle of the antenna with respect to the horizontal plane, $\theta(t)$ the statistical average value of the tilt angle at each data sampling time, including fast-swing variations; ω_s is the average angular rotation velocity and γ_0 the azimuth when the antenna is horizontal. For the altitude range 40–80 km under consideration, the tilt is almost always lower than $15°$ (Karkoschka et al., 2007), so we will use the approximations $\cos \alpha \sim 1$ and $\sin \alpha \sim \alpha$.

We keep the condition that the average amplitude of the vertical component E_V remains almost constant throughout the descent, as for the conventional TM mode, below the upper ionospheric boundary of the cavity (e.g., Sentman, 1990). In addition, the horizontal component must be zero on some perfectly conducting surface under the ground, a condition which is mandatory for having any TM/TE mode. We may ignore here, as a first-order approximation, the presence of the GCR layer, the thickness of which is negligible compared to the wavelength and because of its weak influence on the amplitude of the vertical field on both sides of the layer (Simões et al., 2007). Then, within the atmospheric regions, we can express the ratio E_H/E_V as a linear function $\zeta(h+z_0)$, where ζ is some positive constant proportional to the vertical gradient of the horizontal field, h the altitude and z_0 the depth of the subterranean conducting surface. We apply Eq. (10) to the experimental profile of the signal X plotted in Fig. 1, within two altitude ranges on both sides of the GCR layer. One assumes that for each pair of quasi-simultaneous measurements of PWA and DISR, the tilt angle at the PWA sampling time is statistically equal to the mean value $\theta(t)$ during one rotation. If one integrates Eq. (10) over one rotation of the gondola, the average value obtained for X will be the most probable observed value, as given by

$$\underline{X}(h,t) = Cte \left[\zeta(h+z_0) + \frac{\theta(t)}{T_s} \int_0^{T_s} |\sin(\omega_s t + \gamma_0)| \, dt \right]$$
$$= Cte \left[\zeta(h+z_0) + 2 \frac{\theta(t)}{\pi} \right] \tag{11}$$

where T_s is the spin period.

To smooth the dispersion of the values of θ and $\underline{X}$, we consider the two average values obtained within two samples of 11 measurements each, selected in Table 1 of Karkoschka et al (2007). The first sample corresponds to the average altitude $\underline{h}_1 = 77.8 \, \text{km}$, from MT 1409 s ($\sim 80 \, \text{km}$) to MT 1529 s ($\sim 75 \, \text{km}$), and the second to $h_2 = 41.9 \, \text{km}$, from MT 2564 s ($\sim 48 \, \text{km}$) to MT 3093 s ($\sim 40.5 \, \text{km}$). The fast-swing motions are assumed to be randomly distributed within each sample, since they are of the same duration as the gap δt between PWA and DISR frames (see Section 3.1). We give in Table 1 the average value of $\underline{X}$ of each sample, and the associated average, standard deviation and extreme values of θ_1 (in the region $\underline{h}_1$) and θ_2 (at the region $\underline{h}_2$), as derived from the same files as in Section 3.1. By substituting these values in Eq. (11), we get

$$\frac{\zeta(\underline{h}_1 + z_0) + 2\underline{\theta}_1/\pi}{\zeta(\underline{h}_2 + z_0) + 2\underline{\theta}_2/\pi} = \frac{\underline{X}(\underline{h}_1)}{\underline{X}(\underline{h}_2)} = 4.9 \tag{12}$$

One can check that Eq. (12) has positive solutions for ζ and z_0 only if the inequality $\theta_1 > 4.9\theta_2$ is satisfied. This condition cannot definitely be satisfied in any of the cases, even with the extreme values given in Table 1. If there is no vertical component E_V, the terms with θ disappear, so whatever is the value of z_0, the signal amplitude ratio between the two samples could never be equal to 4.9. Identically, the above inequality may never be satisfied either with the average tilt values in each sample or in the most unlikely situations of the highest tilt ($\theta_1 + \sigma_\theta$) and the lowest ($\theta_2 - \sigma_\theta$). Thus, we must reject the presence of some detectable vertical

component, what confirms the conclusion in Section 3.1. We forsake accordingly the hypothesis of circular polarization of the horizontal component. Additionally, and even more importantly, we must also reject the above proposal of ignoring the influence of the intermediate GCR layer which is thought to be involved with the gradient break of the horizontal electric field component between 80 and 40 km.

5.2. The longitudinal section electric (LSE) mode

We consider now the hypothesis of a horizontal E_H component alone, or at least as the dominating contribution everywhere. We want to check if this hypothesis is compatible with the signal amplitude profile plotted in Fig. 1. We have shown in Section 2.2 that this profile may be fitted satisfactorily with two segments of linear functions, between the surface and about 85 km, with a break at 64 km which corresponds almost to the center of the GCR layer. Over a thickness of about 10 km around this altitude, the conductivity σ_e is larger than $2 \times 10^{-9}\,\mathrm{S\,m^{-1}}$ (Hamelin et al., 2007). For a frequency of 36 Hz, such a conductivity makes the imaginary part of permittivity ($\sigma_e/2\pi\varepsilon_0 f$) larger than the real part ($\varepsilon = 1$). The presence of this layer has been considered in a model for the TM mode (Simões et al., 2007), but to our knowledge there is no model until now for the TE mode with dominant horizontal electric field, neither for Earth nor for Titan. Moreover, considering the actual multi-layer structure imposed by the presence of the GCR layer and of the dielectric ground, we must refer to the general theory developed for dielectric-loaded microwave rectangular waveguides (Collin, 1991). In such a configuration, the interface conditions at the boundaries of each layer cannot be satisfied, in general, by the usual TE and TM modes, but rather by mixing both modes to produce hybrid modes called LSE and longitudinal section magnetic (LSM) modes. There is no electric component perpendicular to the dielectric slabs for LSE modes, and no magnetic component in that direction for LSM modes (Collin, 1991). Thus, the LSE modes comply with the observation of a horizontal electric field component parallel to the slabs. Moreover, the amplitude of E_H must be continuous at the level of each interface. However, the vertical gradient of E_H may change gradually by crossing a non-uniform lossless dielectric layer and one may anticipate that the same phenomenon could happen through an absorbing medium, such as the sudden gradient break observed by crossing the thin GCR layer. We may invoke a simple analogy with the well-known phenomenon of mirages in the atmosphere, where a thin layer of abnormal index of refraction causes horizontal incident optical rays to be refracted and bounced up and down. In our case, even though the variation of the index of refraction through the GCR layer would be relatively weak, we expect a strong influence on waves with tangential incidence and horizontal electric field polarization.

It is beyond the scope of this article to develop the theory of such a particular mode applied to Titan conditions, as it is the subject of forthcoming work. Nevertheless, we may anticipate the main expected results in terms of constraints on the ionospheric conductivity profile and on the location of the underground reflecting surface. Let us consider first, the second portion of the signal profile above the GCR layer, which can be interpreted as perfectly linear in neutral atmosphere. Such linear behavior of horizontal electric field component is predicted by analytical models of Schumann resonance on Earth, for cylindrical geometry (Greifinger and Greifinger, 1978), then for spherical geometry (Sentman, 1990). The difference here is that the straight line plotted in Fig. 1 (portion (ii)) appears to start from a virtual altitude around 51 km, instead of the surface. We may nevertheless assume that the wave properties are essentially deter-

mined hereabout by the conductivity profile of the standard ionosphere above the GCR layer. For LSE modes, the horizontal electric field amplitude is derived from the solution of the Helmoltz differential equation in the vertical direction for the magnetic Hertzian potential (Collin, 1991). This equation is similar to that involving the scalar potential of the Earth's Schumann resonance in region of significant conductivity (Greifinger and Greifinger, 1978), and it simplifies to Bessel's equation yielding the following approximate solutions:

$$|\varphi| \approx \frac{z}{\pi\xi}\left(\frac{z_2 - z_1}{z_1}\right) = \left|\frac{\ln 4k_0^2\xi^2}{\pi}\right|\frac{z}{z_1}; \quad \frac{\partial\varphi}{\partial z} = \left|\frac{\ln 4k_0^2\xi^2}{\pi z_1}\right|$$

$$\text{for} \sim 65\,\mathrm{km} < z \leqslant z_1$$

$$|\varphi| \approx \frac{z_2 - z}{\pi\xi} = \left|\frac{\ln 4k_0^2\xi^2}{\pi}\right| - \frac{z - z_1}{\pi\xi}; \quad \frac{\partial\varphi}{\partial z} = -\left|\frac{1}{\pi\xi}\right|$$

$$\text{for } z_1 \leqslant z \leqslant z_2 \tag{13}$$

where φ is a function of altitude, proportional to the electric field amplitude, z_1 is the altitude where the imaginary part of the complex permittivity at 36 Hz is equal to 1 (i.e., $\sigma_e = \omega\varepsilon_0 = 2 \times 10^{-9}\,\mathrm{S\,m^{-1}}$), z_2 is the upper altitude where all field components become evanescent (i.e., $\sigma_e = 1/4\mu_0\omega\xi^2$), and ξ is the scale height of the conductivity.

Here, all attitudes are referred to the virtual ground ($z \sim 51\,\mathrm{km}$) pointed out by linear extrapolation of the signal amplitude profile below 70 km. Then, we may try to fit the above analytical model to the experimental profile on each side of the altitude of the maximum signal strength ($\sim 90\,\mathrm{km}$). The latter altitude is assumed to be nearly the altitude z_1 where the analytical model predicts the sign inversion of the gradient, as shown by Eq. (13). We may deduce, therefore, the conductivity scale height ξ from the vertical gradient of the amplitude signal on both sides of the maximum by using the following relation:

$$\frac{(\partial\varphi/\partial z)_{z<z_1}}{(\partial\varphi/\partial z)_{z>z_1}} = \frac{(\partial\underline{X}/\partial h)_{h=80\,\mathrm{km}_1}}{(\partial\underline{X}/\partial h)_{h=100\,\mathrm{km}_1}} = \xi\frac{|\ln 4k_0^2\xi^2|}{z_1 - 51} \tag{14}$$

the solution of which is $\xi = 9.25\,\mathrm{km}$, obtained from the profile of $\underline{X}$ (Fig. 1), and for $z_1 \sim 100\,\mathrm{km}$. The altitude of the upper cut-off boundary is given by the relation $z_2 = z_1 + \xi|\ln 4k_0^2\xi^2|$ after Greifinger and Greifinger (1978), which yields $z_2 \sim 180\,\mathrm{km}$, i.e., nearly the lower region of ion-acoustic turbulence.

Note that the above values are only estimate of average values, assuming a uniform model between the supposed source location and the Huygens landing site. However, even though the values of conductivity obtained by the PWA mutual impedance above 80 km are not fully reliable (Hamelin et al., 2007), their order of magnitude ($\sigma \sim 1$ to $2 \times 10^{-10}\,\mathrm{S\,m^{-1}}$) is compatible with the above estimate of $z_1 \sim 100\,\mathrm{km}$ knowing that the analytical model over-estimates the conductivity of the gradient inversion. Moreover, starting from 80 km with the above value and a conductivity scale height of 9.25 km, as deduced from Eq. (14), one can get $\sigma \sim 10^{-5}\,\mathrm{S\,m^{-1}}$ at 180 km which is surprisingly close to the predictions of Borucki et al. (2006) at this altitude with aerosols and for day-time conditions as during the Huygens descent.

The last point to be interpreted in the frame of the LSE mode for Titan's Schumann resonance is the linear portion of the vertical profile in Fig. 1, below the GCR layer. We retain the average signal amplitude at the break altitude of 64 km ($\underline{X} \sim 0.1\,\mathrm{V}$), where the electron conductivity is $\sigma \sim 2.8 \times 10^{-9}\,\mathrm{S\,m^{-1}}$ (Fig. 3). The latter value is even larger than necessary for the gradient bending predicted by analytical models ($|\mathrm{Im}\,n^2| > 1$). In the zoomed plot of Fig. 3 one can check that the slope of $\underline{X}$ profile decreases immediately after the break altitude, down to a value as low as $\sim 10\%$ over 8 km. That distance corresponds to one scale height in the conductivity profile of the GCR layer below the peak (Fig. 3). It

is noticeable that such conductivity scale height is nearly that of the ionization rate below 80 km, due to cosmic-ray bombardment, as predicted by models (Borucki and Whitten, 2008), although both parameters are apparently not strictly proportional in every condition. Nevertheless, it is not the aim of this paper to comment such issue further.

Just a few km below the gradient break in Fig. 1, as soon as the conductivity becomes negligible, the amplitude of the horizontal electric field continues to decrease linearly, as it ought to do so in the neutral atmosphere, before to vanish at the level of some underground conducting surface. In the crust of ice, according to the MI measurement performed at the surface, the ground conductivity and permittivity are $\sigma \sim 4 \times 10^{-10} \, \mathrm{S \, m^{-1}}$ and $\varepsilon \sim 1.8$, respectively (Grard et al., 2006), so one may assign to that material a refractive index nearly close to 1 at 36 Hz. Provided that the conductivity throughout the crust of ice remain small enough, we may extrapolate the profile in Fig. 1 linearly down to the conductive surface, with the same slope as in the atmosphere. Otherwise, the wave would be refracted downwards and the slope would accordingly dip slightly faster than that derived from the linear extrapolation. At any rate, by taking into account more significantly of the large dispersion of the signal strength in presence of ELF noise, a rough extrapolation of the average profile implies the presence of a perfectly conducting boundary at a depth of a few tens of kilometers only.

5.3. Implications for the interior structure

Although other explanations might be found, the simplest and attractive one is the presence of a subsurface conductive ocean (Sotin and Tobie, 2008). This argument is supported by different studies such as the apparent misregistration of geological features on Titan's surface and models comparing Titan with the Galilean icy satellites, as well as those describing the thermal evolution and interior structure of Titan.

Recently, a consistent misregistration of geological features mapped by the Synthetic Aperture Radar (SAR) during successive Cassini flybys has been reported by Stiles et al. (2008). Most of the misregistration can be accounted for by a non-zero obliquity of Titan, but a residual contribution has been interpreted as a deviation of Titan's spin rate relative to synchronous spin rate (Lorenz et al., 2008). Such a spin-rate variation can be explained by an exchange in angular momentum between the atmosphere and the icy crust, if the latter is decoupled from the interior by an ocean (Tokano and Neubauer, 2005). However, this interpretation is challenged by a recent work by Karatekin et al. (2008) which shows that gravitational coupling between the core and the crust would not allow for such large variations as those observed.

On the other hand, Ganymede and Callisto have global characteristics (mass and radius) very similar to Titan. The magnetometers onboard the Galileo spacecraft detected an induced magnetic field within Callisto which is best interpreted by the presence of liquid water with dissolved electrolytes under the ice crust (Khurana et al., 1998). The magnetic signal recorded around Ganymede is best interpreted as the sum of a permanent dipole field, upon which is superimposed an induced magnetic dipole driven by the time-varying component of the externally imposed magnetic field of Jupiter's magnetosphere (Kivelson et al., 2002). This induced component would come again from a subsurface conducting layer, which is thought to be the subsurface ocean. Detecting an ocean within Titan could also be achieved by magnetic survey. However, the determination of an induced magnetic field is not achievable for several reasons, including the small strength of Saturn's magnetic field at Titan, the very weak variations, because Saturn's magnetic dipole is parallel to its spin axis, the presence of the moon's ionosphere, and the large distance of Cassini spacecraft to Titan's surface, which is imposed by a significant atmospheric drag below 950 km.

Gravity data analysis (Rappaport et al., 2008) can also provide an information about the presence of an ocean by measuring the periodic degree-two mass anomalies variations as Titan rotates around Saturn on its highly elliptical orbit. However, it has become a challenge for the present Cassini mission because of the lost of the Ka band (1 cm wavelength) translator, which makes difficult the calibration of the plasma noise. Adequate gravity and magnetic data will have, therefore, to be obtained during a future-dedicated mission to Titan.

Another way to approach the question of Titan's ocean involves models describing the moon evolution and explaining its high eccentricity and the presence of 3% to 5% methane mass fraction in its dense atmosphere. These models predict the presence of an ocean below an icy crust some tens of km thick (e.g., Tobie et al., 2006 and references therein). The thickness of the icy crust depends on the parameters used in the modeling of heat transfer (e.g., Grasset and Sotin, 1996; Sotin and Tobie, 2004) and on the composition of the ocean (Grasset et al., 2000). Without anti-freezing material, Titan would be completely frozen. If ammonia is present, the crust would only be a few tens of kilometers thick (Grasset et al., 2000). If ammonium sulfate is present, the icy crust could be as thick as 176 km (Grindrod et al., 2008). Ammonia was very likely present in the Saturn's sub-nebulae when Titan accreted (Lunine and Stevenson, 1987; Kuramoto and Matsui, 1994; Mousis et al., 2002). It is believed to be the source of the nitrogen which composes ~96% of Titan's dense atmosphere. It is also likely that a deep ocean would contain nitrogen-bearing ions. The cooling of this ocean leads to a thickening of the icy crust with pure ice freezing at its base, while the ocean becomes more and more enriched in ammonia. This fractionation process is related to the melting properties of mixtures of water and ammonia ices (Lunine and Stevenson, 1987). Such models support the linear extrapolation mentioned in the above Section 5.2. Moreover, one can remark that this extrapolation predicts a conductive layer not thicker than a few tens of km below the surface, which seems to favor the ammonia ocean rather than the ammonium sulfate ocean.

6. Summary and conclusion

In this paper, we have presented new developments in data processing of the ELF measurements performed by the PWA experiment onboard the Huygens Probe, from which we may derive a preliminary model for an unexpected kind of Schumann resonance, adapted to Titan conditions. New insights are given here on a strange 36 Hz signal presented as such in the first reports just after the mission (Fulchignoni et al., 2005; Grard et al., 2006). A preliminary analysis led to the likelihood that the phenomenon could be a plasma-driven Schumann-like resonance, powered by the interaction of Titan with the co-rotating magnetosphere of Saturn, instead of atmospheric lightning, as on Earth (Béghin et al., 2007). As a follow-up to the latter publication, now, we may strengthen significantly our preliminary interpretation.

After having extracted the so-called "36 Hz signal" from the raw-data power spectrum bins, the average vertical profile of the signal amplitude, throughout the descent, reveals a well-defined shape with three linear portions. During the first reliable portion of the profile, below 110 km, the signal amplitude increases until 90 km, then decreases rapidly along the second portion, with a linear slope bending rapidly towards an apparent altitude of 51 km above the surface, before exhibiting a break at around

64 km. The latter altitude corresponds closely to the middle of the GCR layer, which is shown to be the cause of the change of slope in spite of an inconvenient pre-programmed mode change occurring 2 min later. Such a change of slope is now considered to be the major proof that the 36 Hz signal cannot result from mechanical artefacts such as those investigated initially (Béghin et al., 2007), since only electric fields may be affected by an ionized medium. After the break, the last portion of the vertical profile of the signal amplitude decreases linearly, as expected in the air, until reaching an offset value at the surface.

To interpret the entire vertical profile plotted in Fig. 1, we proceeded with a statistical study of the 36 Hz signal character-istics, based upon the assumption that it is the electric field component of a natural wave. Different hypotheses have been scrutinized as soon as the Huygens Probe attitude data was published by Karkoschka et al. (2007). From the statistical studies, we may conclude that the behavior of the 36 Hz signal complies with the electromagnetic properties of a wave with horizontally polarized electric field, without detectable vertical component. The apparent dominating source direction, found using the gondola spin modulation, lies along geographical headings of 30–60° East and/or 90–110° West with respect to the Huygens landing site. In the context of a model where 36 Hz would be the second harmonic of a Schumann resonance (Nickolaenko et al., 2003; Simões et al., 2007; Béghin et al., 2007), and considering the latitude of the landing site (~10° South), we postulate that the main source directions, pointed to by the antenna, could correspond roughly to the reconnection polar regions of the tail currents in Titan's ionosphere. This assumption seems to be supported by the observations of a case study during the T5 Titan flyby by Cassini. The signature of a current sheet system, revealed by the magnetometer at low altitude, in the northern polar region, associated with probable observation of quasi-electrostatic ELF waves, in vicinity of IMB crossings, is considered indeed to be a good pointer to the source regions for the supposed Schumann resonance. Although eventual electromagnetic whistler-mode waves seem to be unable to penetrate downwards more deeply than about 800 km in the ionosphere, a wide region extending down to ~200 km is shown to be extremely favorable for a direct generation of intense ion-acoustic turbulence which is believed to be the major source of atmospheric electromagnetic noise, if not the only one.

From the remarkable characteristics of the 36 Hz signal and the first encouraging inputs from Cassini flybys of Titan, we are able to derive a preliminary theoretical model for an unusual and unique mode of Schumann resonance on Titan, the second harmonic of which would have been observed as a consequence of the particular location of the Huygens landing site. Due to several factors such as excitation and injection mechanisms, absence of revealed lightning activity, presence of the intermediate GCR layer between the regular ionosphere and a supposed underground conductive surface, the conventional TM mode, well known on Earth, appears to be not appropriate here. Moreover, because of the apparent absence of a significant vertical component of electric field, the only conventional mode for Titan's cavity resonance would be a TE mode. However, the configuration imposed by the GCR layer and the observation of two refracted branches on each side leads us to consider instead a LSE mode, a degenerated mode from regular TE. In these conditions, a simple analytical model allows us to constrain both boundaries of the atmospheric cavity. The first constraint deals with the scale height of electron conductivity which is found to be of the order of 9 km in the lower ionosphere above 80 km, and the second one concerns the interior structure. Unless further developments of more sophisticated theoretical models bring new insights on our interpretation, the above analysis provides the strongest argu-ment to support the idea of the presence of an ocean under the Titan's surface. Preliminary estimate of an icy crust not thicker than some tens of kilometers constitutes major complementary information to the probable existence of that ocean.

Appendix A

The conventional linear least squares regression method is not applicable to a periodic function such as $F(\gamma)$ plotted in Fig. 8, which involves two variables: the azimuth γ and the amplitude distribution of the signal x, which is a priori randomly distributed in the temporal domain with respect to the periodicity of γ. Then, one replaces the ordinary correlation coefficient of regression by the correlation ratio $\rho(x, \gamma)$, which is independent of the shape of the function. This ratio plays the same role as the correlation coefficient, with the only difference being that the two variables are not permutable, as in a linear regression. The definition of ρ is the ratio between (i) the variance σ_c^2 of the partial means in each class with respect to the mean of the entire parent sample, and (ii) the variance σ_N^2 of the total parent distribution (e.g., Aïvazian, 1970; Kendall and Stuart, 1969). For each test performed with different values of η, as defined in Section 3.3, the correlation ratio $\rho_{(\eta)}$ is given by the following equation:

$$\rho_{(\eta)}^2(x, \gamma) = \frac{\sigma_c^2}{\sigma_N^2} = \frac{\sum_{c=1}^{N_c} n_c (\underline{x}_c - 1)^2}{N\sigma_N^2} \tag{A1}$$

Here, N_c is the number of classes of azimuth ($N_c = 6$) and n_c the number of data points in each class (about 60 in average), x_c is the mean value of x in the class c, and N is the total number of data points in the parent sample ($N = 360$). We use the same usual procedure as for the confidence level of the correlation coefficient. By introducing in Eq. (A1) the average values of x plotted in Fig. 9a and knowing that $\sigma_N = 0.45$, one finds $\rho_1 = 0.165$ and $\rho_2 = 0.173$ for tests #1 and #2, respectively, i.e., an average value $\rho \approx 0.17$.

Before proceeding with the evaluation of the confidence level of the test results, one can check either such values of correlation ratio result from a random effect or not. It is considered (e.g., Aïvazian, 1970) that if the following condition is satisfied, the probability of a real correlation must be rejected

$$\frac{\rho_{(\gamma)}(N - 2)^{1/2}}{1 - \rho_{(\gamma)}^2} < t_{0.05}(N - 2) \tag{A2}$$

where $t_{0.05}$ $(N-2)$ is the quantile with 95% of probability of a Student's distribution with $(N-2)$ degrees of freedom. With $N = 360$, this value is practically the same as for the normal distribution, then $t_{0.05}$ $(N-2) = 1.67$ according to the usual tables. By substituting in (A2) the average value $\rho \approx 0.17$ derived from

tests #1 and #2, one obtains a threshold equal to 3.2, which is almost a factor of two outside the quantile for 95% probability of a random distribution. This enables us to conclude that our correlation ratio does not result from random variations. We can determine now a confidence interval containing the "true value" of ρ based upon the normal random distribution. For a degree of confidence equal to $100-\alpha$, this interval is given by the following relation (e.g., Aïvazian, 1970):

$$\langle \rho \rangle \approx \underline{\rho} + \frac{\rho(1-\rho^2)}{2N} \pm u_{\alpha/2} \frac{1-\rho^2}{(N-1)^{1/2}} \tag{A3}$$

where $u_{\alpha/2}$ is the quantile of the normalized normal distribution $\Phi(u; 0; 1)$ for a percentage equal to $100-\alpha/2$. With $\alpha = 5$, i.e., $\Phi = 0.975$, usual tables give $u_{\alpha/2} = 1.96$. Thus, the "true" value of the correlation ratio is comprised between 7% and 27% with a confidence level of 95%.

References

Agren, K., et al., 2007. On magnetospheric electron impact ionization and dynamics in Titan's ram-side & polar ionosphere—a Cassini case study. Ann. Geophys. 25, 2359–2369.

Aïvazian, S., 1970. Etude statistique des dépendances, (Russian–French translation). Ed. MIR, Moscou.

Banks, P.M., Kockarts, G., 1973. Aeronomy. Academic Press, NewYork and London.

Béghin, C., 1967. Rocket-borne VLF noise observations during aurora (in French). Ann. Geophys. 23, 275–284.

Béghin, C., et al., 2007. A Schumann-like resonance on Titan driven by Saturn's magnetosphere possibly revealed by the Huygens Probe. Icarus 191, 251–266.

Belyaev, G.G., Schekotov, A.Yu., Shvets, A.V., Nickolaenko, A.P., 1999. Schumann resonances observed using Poynting vector spectra. J. Atmos. Sol.-Terr. Phys. 61, 751–763.

Bertucci, C., Neubauer, F.M., Szego, K., Wahlund, J.-E., Coates, A.J., Dougherty, M.K., Young, D.T., Kurth, W.S., 2007. Structure of Titan's mid-range magnetic tail: Cassini magnetometer observations during the T9 flyby. Geophys. Res. Lett. 34, L24S02.

Bertucci, C., et al., 2008. The magnetic memory of Titan's ionized atmosphere. Science 321, 1475–1478.

Bertucci, C., Sinclair, B., Achilleos, N., Hunt, F., Dougherty, M.K., Arridge, C.S., 2009. The variability of Titan's magnetic environment, Planet. Space Sci., this issue, doi:10.1016/j.pss.2009.02.009.

Besser, B.P., 2007. Synopsis of the historical development of Schumann resonances. Radio Sci. 42, RS2S02.

Blanc, M., et al., 2002. Magnetosphere and plasma science with CASSINI–HUYGENS. Space Sci. Rev. 104, 253–346.

Booker, H.G., 1984. Cold Plasma Waves. Martinus Nijhoff Pub, Dordrecht/Boston/Lancaster, pp. 1–345.

Borucki, W.J., Levin, Z., Whitten, R.C., Keesee, R.G., Capone, L.A., Summers, A.L., Toon, O.B., Dubach, J., 1987. Predictions of the electrical conductivity and charging of the aerosols in Titan's atmosphere. Icarus 72, 604–622.

Borucki, W.J., Whitten, R.C., Bakes, E.L.O., Barth, E., Tripathi, S., 2006. Predictions of the electrical conductivity and charging of the aerosols in Titan's atmosphere. Icarus 181, 527–544.

Borucki, W.J., Whitten, R.C., 2008. Influence of high abundances of aerosols on the electrical conductivity of the Titan atmosphere. Planet. Space Sci.

Bychenkov, V.Yu., Myatt, J., Rozmus, W., Tikhonchuk, V.T., 1994. Quasihydrodynamic description of ion-acoustic waves in a collisional plasma. Physics of Plasmas, edit. American Institute of Physics. Vol. 1(8). Melville, NY, USA, 2419–2429.

Collin, R.E., 1991. Field Theory of Guided Waves, Second ed. IEEE Inc., New York, pp. 1–852.

Dougherty, M.K., et al., 2004. The Cassini magnetic field investigation. Space Sci. Rev. 114, 331–383.

Fischer, G., Kurth, W.S., Dyudina, U.A., Kaiser, M.L., Zarka, P., Lecacheux, A., Ingersoll, A.P., Gurnett, D.A., 2007. Analysis of a giant lightning storm on Saturn. Icarus 190, 528–544.

Fulchignoni, M., et al., 2002. The characterization of Titan's atmospheric physical properties by the Huygens Atmospheric Structure Instrument (HASI). Space Sci. Rev. 104, 395–431.

Fulchignoni, M., et al., 2005. In situ measurements of the physical characteristics of Titan's environment. Nature 438/8, 785–791 doi: 1038/nature04314.

Grard, R., Svedhem, H., Brown, V., Falkner, P., Hamelin, M., 1995. An experimental investigation of atmospheric electricity and lightning activity to be performed during the descent of the Huygens Probe on Titan. J. Atmos. Terr. Phys. 57, 575–585.

Grard, R., et al., 2006. Electric properties and related physical characteristics of the atmosphere and surface of Titan. Planet. Space Sci. 54, 1124–1136.

Grasset, O., Sotin, C., 1996. The cooling rate of a liquid shell in Titan's interior. Icarus 123, 101–112.

Grasset, O., Sotin, C., Deschamps, F., 2000. On the internal structure and dynamics of Titan. Planet. Space Sci. 48, 617–636.

Greifinger, C., Greifinger, P., 1978. Approximate method for determining ELF eigenvalues in the earth-ionosphere waveguide. Radio Sci. 13, 831–837.

Grindrod, P.M., Fortes, A.D., Nimmo, F., Feltham, D.L., Brodholt, J.P., Vocadlom, L., 2008. The long-term stability of a possible aqueous ammonium sulfate ocean inside Titan. Icarus 197, 137–151.

Gurnett, D.A., Scarf, F.L., Kurth, W.S., 1982. The structure of Titan's wake from plasma wave observations. J. Geophys. Res. 87, 1395–1403.

Gurnett, D.A., et al., 2004. The Cassini radio and plasma wave investigation. Space Sci. Rev. 114, 395–463.

Hamelin, M., et al., 2007. Electron conductivity and density profiles derived from the mutual impedance probe measurements performed during the descent of Huygens through the atmosphere of Titan. Planet. Space Sci. 55, 1964–1977.

Hamelin, M., Grard, R., López-Moreno, J.J., Schwingenschuh, K., Béghin, C., Berthelier, J.J., Simões, F., 2009. Comment on "Evidence of electrical activity on Titan drawn from the Schumann resonances sent by Huygens probe". by Morente, J.A., Portí, J.A., Salinas, A., Navarro, E.A. [doi:10.1016/j.icarus.2008.02.004]. Icarus (2009), doi:10.1016/jicarus.2009.01.031.

Hartle, R.E., Sittler Jr., E.C., Ogilvie, K.W., Scudder, J.D., Lazarus, A.J., Atreya, S.K., 1982. Titan's ion exosphere observed from Voyager 1. J. Geophys. Res. 87, 1383–1394.

Hayakawa, M., Tanaka, Y., Iwai, A., Ohtsu, J., Storey, L.R.O., Béghin, C., Jorgensen, T.S., 1981. Simultaneous spaced direction-finding measurements of medium-latitude VLF/ELF emissions. Planet. Space Sci. 29, 505–520.

Jernej, I., Falkner, P., 2004. HASI-PWA Calibration Document, HASI-PWA-FM-DOC-41, Institut fuer Weltraumforschung. Austrian Academy of Science, Issue draft, Rev.1.

Karatekin, O., Van Hoolst, T., Tokano, T., 2008. Effect of internal gravitational coupling on Titan's non-synchronous rotation. Geophys. Res. Lett. 35, L16202.

Karkoschka, E., Tomasko, M.G., Doose, L.R., See, C., McFarlane, E.A., Schröder, S.E., Rizk, B., 2007. DISR imaging and the geometry of the descent of the Huygens Probe within Titan's atmosphere. Planet. Space Sci. 55, 1896–1935.

Kendall, M.G., Stuart, A., 1969. The Advanced Theory of Statistics, Vol. 3. Charles Griffin & co, London.

Khurana, K.K., Kivelson, M.G., Stevenson, D.J., Schubert, G.C., Russel, T., Walker, R.J., Polanskey, C., 1998. Induced magnetic fields as evidence for subsurface oceans in Europa and Callisto. Nature 395, 777–780.

Kivelson, M.G., Khurana, K.K., Volwerk, M., 2002. The Permanent and Inductive Magnetic Moments of Ganymede. Icarus 157, 507–522.

Kuramoto, K., Matsui, T., 1994. Formation of a hot proto-atmosphere on the accreting giant icy satellite: Implications for the origin and evolution of Titan, Ganymede, and Callisto. J. Geophys. Res. 99, 21183–21200.

Labendz, D., 1998. Investigation of Schumann resonance polarization parameters. J. Atmos. Sol.-Terr. Phys. 60, 1779–1789.

Lammer, H., Tokano, T., Fischer, G., Stumptner, W., Molina-Cuberos, G.J., Schwingenschuh, K., Ruckeret, H.O., 2001. Lightning activity on Titan: can Cassini detect it? Planet. Space Sci. 49, 561–574.

Lebreton, J.P., et al., 2005. An overview of the descent and landing of the Huygens probe on Titan. Nature 438, 758–764.

Löpez-Moreno, J.J., et al., 2008. Structure of Titan's low altitude ionized layer from the Relaxation Probe aboard HUYGENS. Geophys. Res. Lett. 35, 222104.

Lorenz, R.D., Stiles, B.W., Kirk, R.L., Allison, M.D., Persi del Marmo, P., Iess, L., Lunine, J.I., Ostro, S.J., Hensley, S., 2008. Titan's rotation reveals an internal ocean and changing zonal winds. Science 319 (5870), 1649–1651.

Lunine, J.I., Stevenson, D.J., 1987. Clathrate and ammonia hydrates at high pressure: application to the origin of methane on Titan. Icarus 70, 61–77.

Merlino, R.L., 1997. Current-driven dust ion-acoustic instability in a collisional dusty plasma. IEEE Trans. Plasma Sci. 25, 60–65.

Modolo, R., Wahlund, J.-E., Bostrom, R., Canu, P., Kurth, W.S., Gurnett, D., Lewis, G.R., Coates, A.J., 2007. Far plasma wake of Titan from the RPWS observations: a case study. Geophys. Res. Lett. 34, L24S04.

Molina-Cuberos, G.J., López Moreno, J.J., Lara, L.M., Rodrigo, R., O'Brien, K., 1999. Ionization by cosmic rays of the atmosphere of Titan. Planet. Space Sci. 47, 1347–1354.

Molina-Cuberos, G.J., Porti, J., Besser, B.P., Morente, J.A., Margineda, J., Lichtenegger, H.I.M., Salinas, A., Schwingenschuh, K., Eichelberger, H.U., 2004. Schumann resonances and electromagnetic transparence in the atmosphere of Titan. Adv. Space Res. 33, 2309–2313.

Morente, J.A., Porti, J.A., Salinas, A., Navarro, E.A., 2008. Evidence of electrical activity on Titan drawn from the Schumann resonances sent by Huygens probe. Icarus 195, 802–811.

Mousis, O., Gautier, D., Bockelée-Morvan, D., 2002. An evolutionary turbulent model of Saturn's subnebula: implications for the origin of the atmosphere of Titan. Icarus 156, 162–175.

Neubauer, F.M., et al., 2006. Titan's near magnetotail from magnetic field and electron plasma observations and modeling: Cassini flybys TA, TB, and T3. J. Geophys. Res. 111, A10220.

Nickolaenko, A.P., Besser, B.P., Schwingenschuh, K., 2003. Model computations of Schumann resonance on Titan. Planet. Space Sci. 51, 853–862.

Rappaport, N.J., Iess, L., Wahr, J., Lunine, J.I., Armstrong, J.W., Asmar, S.W., Tortora, P., Di Benedetto, M., Racioppa, P., 2008. Can Cassini detect a subsurface ocean in Titan from gravity measurements? Icarus 194, 711–720.

Schumann, W.O., 1952. Über die strahlungslosen Eigenschwingungen einer leitenden Kugel, die von einer Luftschicht und einer Ionosphärenhülle

umgeben ist, (On the free oscillations of a conducting sphere which is surrounded by an air layer and an ionosphere shell). Z. Naturfors. 7a, 149–154.

Scott, D., 1985. Averaged shifted histograms: effective nonparametric density estimators in several dimensions. Ann. Stat. 13 (3), 1024–1040.

Sentman, D.D., 1990. Approximate Schumann resonance parameters for a two-scale height ionosphere. J. Atmos. Terr. Phys. 52, 35–46.

Shukla, P.K., 1986. Nonlinear stability of ion-acoustic waves. Phys. Rev. A 34, 644–646.

Simões, F., et al., 2007. A new numerical model for the simulation of ELF wave propagation and the computation of eigenmodes in the atmosphere of Titan: did Huygens observe any Schumann resonance? Planet. Space Sci. 55, 1978–1989.

Sotin, C., Tobie, G., 2004. Internal structure and dynamics of the large icy satellites. C. R. Acad. Sci. Phys. 5, 769–780.

Sotin, C., Tobie, G., 2008. Titan's Hidden Ocean. Science 319 (5870), 1629–1630.

Stiles, B.W., Cassini RADAR Team, et al., 2008. Determining Titan's spin state from Cassini RADAR images. Astron. J. 135, 1669–1680.

Swanson, D.G., 1989. Plasma Waves. Academic Press Inc., Boston, New York, London.

Tobie, G., Lunine, J., Sotin, C., 2006. Episodic outgassing as the source of atmospheric methane on Titan. Nature 440, 61–64.

Tokano, T., Neubauer, F., 2005. Wind-induced seasonal angular momentum exchange at Titan's surface and its influence on Titan's length-of-day. Geophys. Res. Lett. 32, L24203.

Tomasko, M.G., et al., 2005. Rain, winds and haze during the Huygens Probe's descent to Titan surface. Nature 438/8, 765–778.

Wahlund, J.-E., et al., 2005. Cassini measurements of cold plasma in the ionosphere of Titan. Science 308, 986–989.

Yair, Y., Fisher, G., Simões, F., Renno, N., Zarka, P., 2008. Updated review of planetary atmospheric electricity. Space Sci. Rev. 137, 29–49.